Magnetic ordering in ultrasmall potassium ferrite nanoparticles grown on graphene nanoflakes

Ferdinand Hof,[†,*] Lorenzo Poggini,[‡] Edwige Otero,[§] Benoît Gobaut,[§] Mathieu Gonidec,[‡] Mathieu Duttine,[‡] Patrick Rosa,[‡,*] Olivier Sandre,[♯] Alain Pénicaud[†]

† Univ . Bordeaux, CNRS, Centre de Recherche Paul Pascal, UMR5031, 33600 Pessac, France

‡ Univ. Bordeaux, CNRS, Bordeaux-INP, ICMCB, UMR 5026, F-33600 Pessac, Cedex

§ Synchrotron SOLEIL, L'Orme des Merisiers Saint Aubin, BP 48 F-91192 Gif sur Yvette,France

♯ Univ. Bordeaux, CNRS, Bordeaux INP, LCPO, UMR-5629, F-33600, Pessac, France

Keywords: potassium ferrites, ultrasmall nanoparticles, nanocomposite, graphene nanoflakes

Supporting Information Placeholder

ABSTRACT: Magnetic nanoparticles are central to the development of efficient hyperthermia treatments, magnetic drug carriers, and multimodal contrast agents. While the magnetic properties of small crystalline iron oxide nanoparticles are well understood, the superparamagnetic size limit constitutes a significant barrier for further size reduction. Iron (oxy)hydroxide phases, albeit very common in the natural world, are far less studied, generally due to their poor crystallinity. Templating ultra-small nanoparticles on substrates such as graphene is a promising method to prevent aggregation, typically an issue for both material characterization as well as applications. We generate ultra-small nanoparticles, directly on the carbon framework by the reaction of potassium graphenide solution, charged graphene flakes, with iron(II) salts. After mild water oxidation, the obtained composite material consists of ultrasmall potassium ferrite nanoparticles, bound to the graphene nanoflakes. Magnetic properties as evidenced by magnetometry and X-ray Magnetic Circular Dichroism, with open magnetic hysteresis loops near room temperature, are widely different from classical ultra-small superparamagnetic iron oxide nanoparticles. The large value obtained for the effective magnetic anisotropy energy density K_{eff} accounts for the presence of magnetic ordering at rather high temperatures. The synthesis of ultra-small potassium ferrite nanoparticles in such mild conditions is remarkable given the harsh conditions used for the classical syntheses of bulk potassium ferrites. Moreover, the potassium incorporation in the crystal lattice occurrs in the presence of potassium cations under mild conditions. A transfer of this method to related reactions would be of great interest, which underlines the synthetic value of this study. These findings also shed new light on the previously reported electro-catalytic properties of those nanocomposite materials, especially for the sought-after oxygen reduction/evolution reaction. Finally, their longitudinal and transverse proton NMR relaxivities when dispersed in water were assessed at 37°C under a magnetic field of 1.41T, allowing potential applications in biological imaging.

Introduction: Developing and exploiting size calibrated magnetic nanoparticles (mnPs) has been envisioned to improve the current state of technology in a wide range of disciplines e.g. catalysis, biomedicine, magnetic resonance imaging, and data storage.[1–5] For every ferromagnetic material, a certain domain size limit exists, varying typically between 10 to more than 100 nm,[6,7] below which superparamagnetism is observed. For nanoparticle the size of which is less than a magnetic domain size, the energy to maintain different domain sizes is too large. Consequently each nanoparticle behaves like a giant paramagnetic atom, exhibiting i) large constant magnetic moment, ii) fast response to applied magnetic fields, iii) negligible remanence and coercivity. Moreover, shape, exact composition, and magneto-crystalline anisotropy are also critical parameters that influence the magnetic properties, due to the interplay between finite-size effects, surface anisotropy, and spin disorder.[8]

Iron oxides are among the most studied magnetic materials, due to their high natural abundance, low price, superior bio-compatibility, and technological importance.[9] They exist in a wide range of compositions and polymorphs, e.g Fe_3O_4, γ-Fe_2O_3, exhibiting typically good crystallinity and well-defined structures both in the bulk phase and as nanoparticles. For small nanoparticles superparamagnetism is observed in poorly ordered ferrihydrite ($Fe_5HO_8{\cdot}4H_2O$), ~~in~~ the naturally occurring mineral feroxyhyte (δ'-FeOOH), and in synthetic nanoparticles of hematite (<8 nm), magnetite (<10-15 nm), maghemite and antiferromagnetic goethite (<15-20 nm).[9]

Sintering at high temperatures (typically 1000 °C and above) of iron oxides or (oxy)hydroxides with alkali or alkaline earth metals leads to ferrites, such as the hard hexagonal ferrites $AFe_{12}O_{19}$ (A= Ba, Sr). For potassium ferrites,[10] a variety of ternary phases have been described in the literature,[11] exhibiting some unusually high oxidation states such as in K_2FeO_4, K_3FeO_4, and K_2FeO_3.[12] The more typical Fe(II)/Fe(III) states can be found: in potassium ferrites such as $KFeO_2$,[13,14] $K_6Fe_2O_6$,[15] $K_{14}Fe_4O_{13}$,[16] and a variety of different phases with the general composition $K_2O{\cdot}nFe_2O_3$: $K_2Fe_4O_7$[17] and K-β-ferrite $K_2Fe_{22}O_{34}$.[18] For stoichiometrically pure phases containing only Fe(III), several compounds are known such as $K_{2+x}Fe_{22}O_{34}$, K-β-"-ferrite $K_4Fe_{22}O_{34}$,[11] and recently, the mixed oxo-hydroxoferrate $K_{2-x}Fe_4O_{7-x}(OH)_x$.[19] While orthorhombic $KFeO_2$ is an antiferromagnet, comprised of infinitely linked Fe^{3+} O_4^{2-} tetrahedra,[13] $K_xFe_{22}O_{34}$ has a hexagonal layered structure, with spinel-like ferrimagnetic blocks $-(O_4Fe_3)_3-O_4-$comprised of both tetrahedral and octahedral iron atoms ~~like~~ as in Fe_3O_4. These layers are separated and coupled antiferromagnetically by [FeO_4] pillars, enclosing cavities where potassium cations are located and surrounded by nine oxygen atoms.[19–21] The K-content can be modulated either by increasing the thickness of the spinel blocks, thus continuously approaching pure Fe_3O_4, or directly by a variation in the occupation of the K_xO sublayers. Surprisingly, while extensive efforts have been devoted to the synthesis in mild conditions of small to ultrasmall nanoparticles of a vast variety of ferrites, very few results have been published on potassium ferrites. The only report is on $KFeO_2$ nanoparticles about 5.5-6.0 nm in size.[22] Antiferromagnetism and opening of a magnetic hysteresis at room temperature, with a saturation moment of 0.58 μ_B/Fe at 1.5 T were observed. This scarce interest in nanoscale downsizing of

such compounds is all the more surprising given their utility in a variety of catalytic processes and as solid-state electrolytes.[11,18,19,23–28]

Carbon templated magnetic nanoparticles[29–31] are sought after for biological applications such as magnetic and combined magnetic-photonic hyperthermia treatment,[32] magnetic drug carriers,[33] or multimodal contrast agents for bioimaging,[34] ǂ and as negative contrast agents in magnetic resonance imaging (MRI).[35,36] Recently, some of us have reported the synthesis of 2-5 nm diameter iron oxide/hydroxide nanoparticles grafted to the framework of graphitic nano carbons (Fe(nP)/nC),[37,38] by exploiting the low reduction potential of graphenide solutions.[39,40] Graphenide solutions can be obtained upon dissolving potassium intercalated graphite or graphitic nanocarbons and are stable under inert conditions, and in aprotic solvents.[41–49] Graphenide solutions are strong reducing agents and have been used to graft functional moieties covalently to the carbon framework.[50–52] By the addition of anhydrous metal salts (here $[Fe(BF_4)_2(THF)_x]$), a charge transfer from the graphene sheet to the metal cations occurs, leading presumably to the formation of zero-valent iron metal nanoparticle attached to the carbon framework. The subsequent workup in water outside of the glovebox led to the oxidation of these nanoparticles, which remained tethered to the nanocarbon framework.[53] This nanocomposite was found to be a highly-performing bi-functional catalyst for the oxygen reduction and oxygen evolution reaction. The versatility of this chemical platform is highlighted by the fact that virtually every d block metal salt may be reduced by graphenide, forming nanoparticles about 2-5 nm in diameter, grafted onto the nano-graphene sheets.[40,54]

In our previous work, [53] we argued that the oxidation of graphenide solutions by ferrous cations leads to the decoration of the graphene nanosheets by iron oxide or (oxy)hydroxide nPs. In the present contribution, the magnetic properties of the Fe(nP)/nC nanocomposite have been studied in detail by a combination of techniques: Mössbauer spectroscopy, magnetometry, Fe L-edge X-ray absorption spectroscopy, and proton NMR relaxometry. As a result, remarkable magnetic properties have been observed, which are unusually strong for mnPs of such small sizes. After re-evaluation and refinement of the structural characterization, with detailed HR-TEM, ICP-OES, XPS analysis corroborated by Fe L-edge X-ray absorption spectroscopy, the composition for the composite material was determined to be closer to potassium ferrites than pure iron oxide or (oxy)hydroxide. Such alkali metal ferrites are usually obtained in much harsher conditions upon calcination.[10] In contrast, the oxidation step of the nanoparticles here occurs at room temperature, once removed from the inert gas atmosphere, by a simple aqueous workup. Arguably, the presence of potassium cations in the course of the workup leads to the incorporation of those cations in the nanoparticle crystal structure. This finding allows the generation of potassium ferrites under mild conditions and highlights the synthetic value of the underlying synthetic strategy. Moreover, this study provides a detailed picture on those composite materials and indicates why they have proven to be excellent electrocatalysts for the oxygen reduction and oxygen evolution reactions, [39] and, similarly to other carbon templated iron oxide nanoparticles, promising candidates for biological applications such as magnetic hyperthermia, magnetic drug carriers, or multimodal contrast agents for bioimaging.

Results:

The grafting to the nanocarbon flakes was performed according to a literature procedure (Scheme 1). We had previously estimated the amount of iron in the composite material to be between 2.5 and 3 at% by TGA, assuming that the combustion residue was α-Fe_2O_3 (hematite) after TGA measurement up to 750 °C.[39]

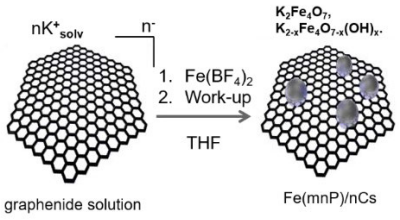

Scheme 1 Reaction of the graphenide solution, generated by the dissolution of potassium graphite intercalation compounds (KC_8) in THF with dissolved $Fe(BF_4)_2$. Magnetic iron nanoparticles are found on the carbon framework, exhibiting a composition close to $K_2Fe_4O_7$, or $K_{2-x}Fe_4O_{7-x}(OH)_x$ (synthetic details can be also be found in ref [39])

Magnetic characterization was subsequently carried out, and the main result was magnetic ordering at room temperature. This observation is truly surprising since such ultrasmall nanoparticles are expected to be superparamagnetic and show freezing of the spin domains at much lower temperatures (e.g. below ~10-15 K for <3 nm nanoparticles of maghemite,[55,56] maghemite/magnetite,[57] iron,[58] cobalt ferrite[59], or manganese ferrite[60]). We investigated further the magnetic behavior of those Fe(nP)/nC nanocomposites ~~at~~ in the bulk through standard magnetometry (further details in ESI). A preliminary XPS survey confirmed, as previously seen,[39] a preponderance of O, C, and Fe. The small amount of Si observed is likely adventitious contamination originating from ~~an~~ etching of the glassware by the fluorinated anion as previously observed (see Figure S1. in Supporting Information (ESI)).[61]; After careful evaluation, we also determined the presence of residual K, but its low cross-section at the Al K_α energy prevented a reliable quantification. High-resolution O 1s, Fe 2p, and Fe 3p spectra were obtained and after background subtraction with the corresponding Shirley functions, deconvolution with the Gupta and Sen multiplet structure corresponding to Fe(III)[62–64] yielded satisfactory fits (see Figure S2). The resulting peaks and their attribution in light of the literature for iron oxides[62–64] and hydroxides[65] are reported in Table S1 (ESI). The absence of peaks below 55 eV for Fe 3p and below 710 eV for the Fe 2p spectra[63–65] confirms that the iron is exclusively in oxidation state (III), without any traces of Fe(II) or residual Fe(0).[64] Meanwhile, the O 1s spectrum evidences the presence of a lattice hydroxyl peak 1.1 eV above the lattice oxide main peak.

Chemical characterization (Inductively-Coupled Plasma Optical Emission Spectroscopy, ICP-OES**):**

We measured the content of Fe, B, and K of solutions resulting from the complete digestion of the Fe(nP)/nC nanocomposites (see Experimental Section). No residual boron content was quantified, confirming that the work-up step successfully removes the expected by-product of the oxidation reaction, KBF_4. Nevertheless, potassium itself was not completely removed in agreement with the XPS survey. More surprisingly, we found that the potassium content was not negligible, amounting to 3.2% w/w. The iron content was found to be 8.5%, instead of the 16.7% derived from TGA assuming the combustion residue to be α-Fe_2O_3. Accordingly, the ICP analysis of the TGA residues showed Fe contents at 47.4%, well below the 69.9% expected for Fe_2O_3. Overall, the atomic ratio Fe/K is close to 2. A XRD diffractogram was obtained on the TGA combustion residue before the ICP digestion (Figure 1). Despite the unfavorable signal-to-noise ratio, the measured diffraction pattern shows that hematite is present together with another phase that corresponds nicely to $K_2Fe_{22}O_{34}$.

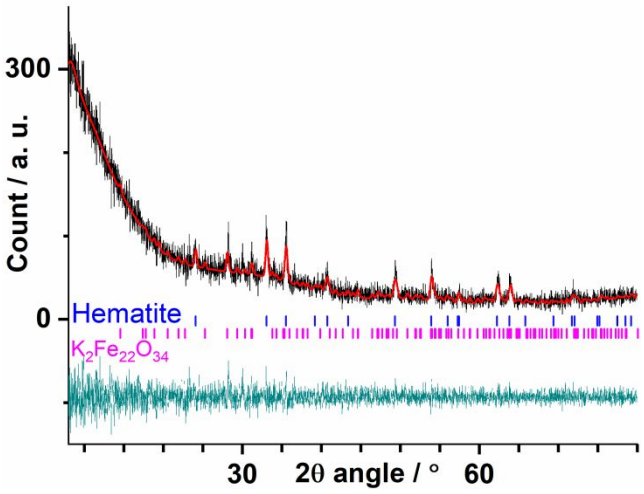

Figure 1. Powder diffractogram of the TGA combustion residue (black line), with a profile-matching simulated diffractogram (red line) using the cif files of hematite (Bragg peak positions in blue) and $K_2Fe_{22}O_{34}$ (Bragg peak positions in violet), with residual plotted in dark cyan. ICP analysis of this residue yielded 29.8(3)% Fe and 12.1(1)% K. No satisfactory combination of only hematite and $K_2Fe_{22}O_{34}$ fitted those values.

We reinvestigated more precisely the size distribution of the nanoparticles by means of high-resolution transmission electron microscopy (HR-TEM) analysis.[39,40] It must be stressed that those objects are particularly difficult to image correctly given the strong tendency of the graphene nanoflakes to aggregate during reaction. After some optimization, drop-casting the suspension resulting from sonication in THF allowed us to record about 40 images of the composite materials containing randomly orientated, aggregated carbon layers and iron containing nanoparticles (see Figure 2a as a representative picture). The sizes of 137 individual Fe(nP) (see Figure 2b) yielded the frequency histogram in Figure 2c. By fitting the histogram with a log-normal distribution, the average particle size has been determined to be 2.8 nm, with a characteristic width σ_{TEM} =0.1. These results agree well with the previously estimated sizes between 2-5 nm.[39] The standard deviation is only about 0.3 nm, allowing us to conclude that this reaction provides well sized calibrated nanoparticles, which are bound to the basal plane of the carbon nanomaterial. It must be stressed that the nanoparticles shown indeed contain iron, as was previously shown by EELS and EDX measurements.[39,40]

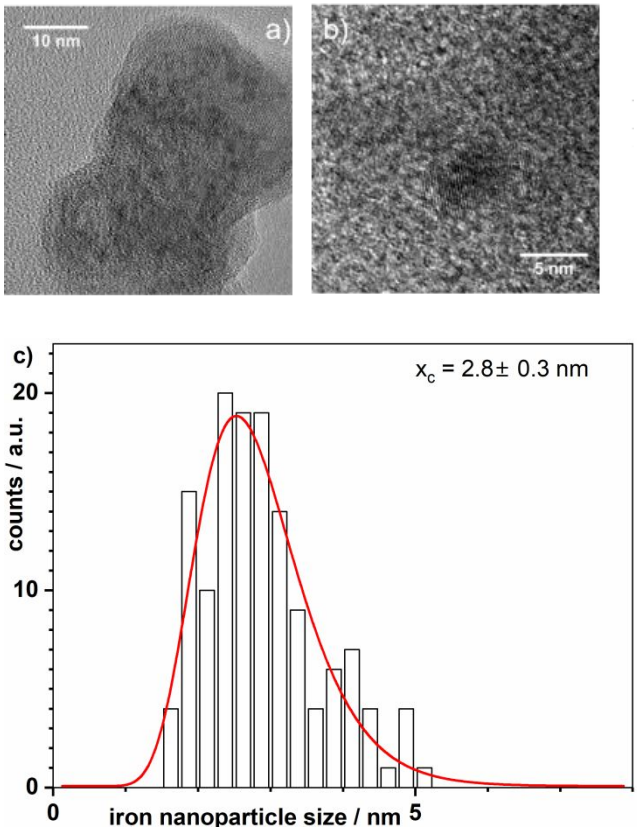

Figure 2. a) HR-TEM images of the composite material Fe(nP)/nC; b) close-up on one Fe(nP) nanoparticle; c) histogram of the size distribution of iron nanoparticles, shown to be centered at 2.8±0.3 nm based on a log-normal fitting of the data of (non-dimensional) width parameter σ=0.1

Mössbauer spectroscopy:

Semi-quantitative Mössbauer spectra were measured on the Fe(nP)/nC nanocomposite. Spectra obtained at room temperature and 4 K (Figure 3) show the occurrence of magnetic ordering, and fits were attempted considering either quadrupolar or hyperfine magnetic field splitting distributions, reflecting in part the poor signal-to-noise ratio but also a likely variation in the local Fe surroundings (values reported in Table S2). Isomeric shifts for both components corroborate the presence of Fe(III) evidenced by XPS analysis. The spectrum at 4.2 K is slightly improved, and can be fitted with two very close sextets: isomeric shifts are around 0.5 mm/s, quadrupole splitting close to zero and hyperfine magnetic fields distributed around 44 and 51 T.

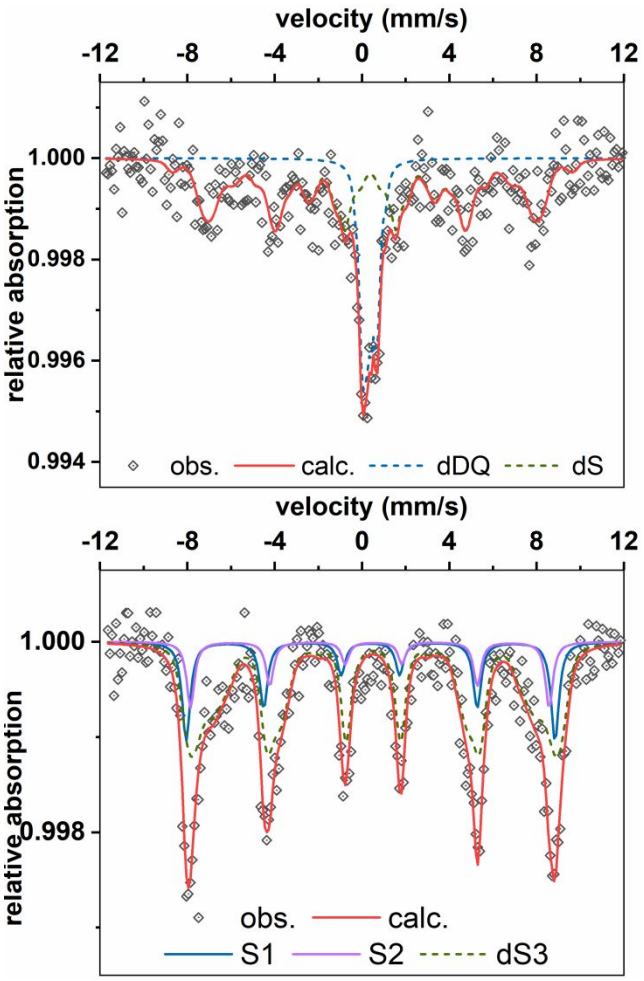

Figure 3. Transmission ^{57}Fe Mössbauer spectra of Fe(nP)/nC at 293K (top) and 4.2K (bottom), with experimental data (black circles), total calculated spectra (red line), and the two individual components (green and blue dotted lines, see table S2 in ESI).

Magnetometry:

The Zero-Field Cooled/Field Cooled (ZFC-FC) measurement on one batch of the Fe(nP)/nC nanocomposite is presented in Figure 4. These ultrasmall nanoparticles start showing magnetic ordering at a surprisingly high temperature, evidenced by the divergence of the two curves below 339±1K. This is the so-called irreversibility temperature, T_{irr}, below which the superparamagnetic giant spins start freezing in the largest nanoparticles of the distribution. The ZFC magnetization curve is seen to increase with temperature, reaching a quite flat maximum at T_{max} = 110±5K. This maximum should correspond to the freezing of spins for the nanoparticles of the most abundant size. This T_{max} temperature is related to the average blocking temperature T_B,[66] that is the temperature for which the superparamagnetic relaxation time corresponds to the experimental time window. With $T_{max} = \beta\langle T_B\rangle$, with the proportionality constant $\beta = 2$, we have thus T_B = 55 K. With $\langle K_{eff}\rangle = k_B T_B \ln(\tau_m f_0)/\langle V\rangle$, taking the average volume $\langle V\rangle$ from the TEM measurements, the frequency factor f_0 estimated at 10^9 s^{-1},[67] and the characteristic measurement time τ_m = 50 s, we can estimate an effective anisotropy constant for the nanocomposite $\langle K_{eff}\rangle = 1.6 \times 10^6$ Jm^{-3}. This value is much higher than anisotropy constant values for pure iron oxide nPs which are typically in the 5×10^3–1.5×10^4 Jm^{-3} range (e.g. see nanoparticles between 2.5 and 16nm, see [56,68,69]).

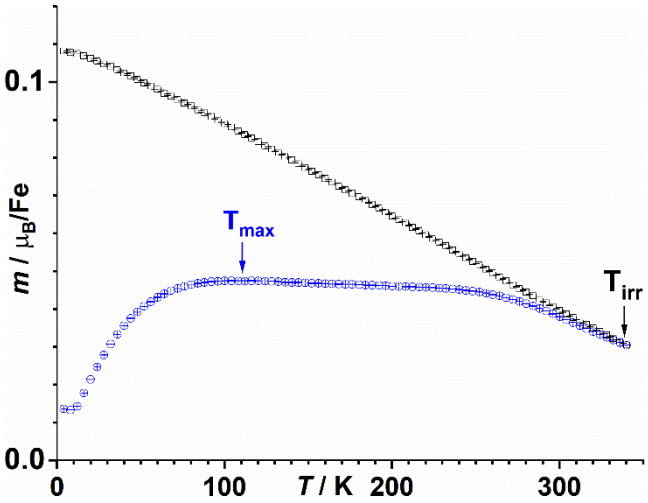

Figure 4. Zero-Field Cooled/Field Cooled (blue circles and black squares respectively) measured under 5 mT for Fe(nP)/nC.

Evidence of a slight evolution of magnetic properties at temperatures above ambient conditions is found in the isothermal magnetization curves measured at and above room temperature (Figure S3). Indeed, below 300 K hysteresis loops describe fully closed symmetrical curves with symmetrical saturation values, from 300 to 350 K. While the hysteresis loops appear to open up around zero field they fail to describe closed curves at high field. This change in the nanocomposite may certainly be linked to the presence of surface and structural hydroxyl groups and water moieties that can be removed at high temperatures, which would account for the alteration of the magnetic properties. A similar evolution was seen with time, with measurements performed after two months on a sample from the same batch (kept at room temperature), up to only 250 K to avoid the evolution previously seen (labelled forthwith 2nd measurement). In the ZFC-FC curve, divergence occurred only at about 250 K (Figure S4). The observed behavior was nonetheless similar, the difference in the maximum of the ZFC curve at T_{max} = 103±1 K being small, the blocking temperature T_B = 52 K, and the derived effective anisotropy constant $\langle K_{eff}\rangle = 1.5 \times 10^6$ Jm^{-3} are almost unchanged.

The field dependence of the magnetization, measured between 1.8 and 250 K on the aged sample (Figure 5), evidenced opening of the hysteresis loops below 250 K. Hysteresis loop opening has also been observed on somewhat larger $KFeO_2$ nanoparticles (4 to 7 nm).[22]

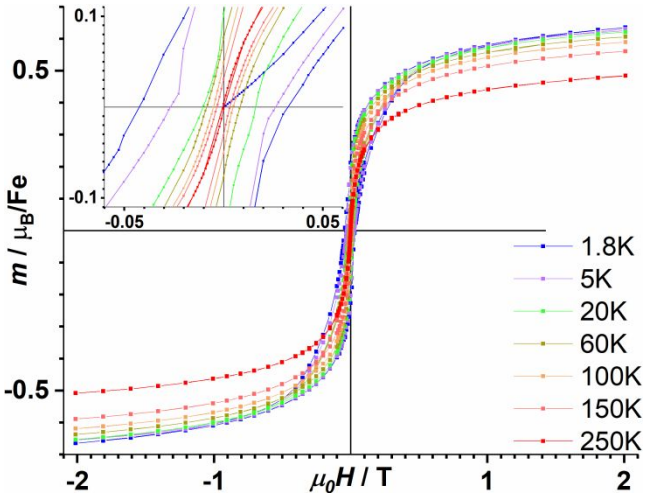

Figure 5. Field dependence of the magnetization for Fe(nP)/nC

measured between 1.8 and 250 K (in step mode). Inset: close-up in the low-field region showing the opening of the hysteresis loops.

While coercive field H_c and remnant magnetization M_r are readily extracted from the curve, the saturation magnetization value M_S was extracted from a fit using the law of approach to saturation (LAS, see full discussion in ESI):[70]

$$M(T,H) = M_S(T)\left[1 - \frac{b}{H^2}\right] + \chi_0(T)H$$

The values of M_S, M_r and $\mu_0 H_c$, together with b and $\chi_0(T)$ are reported in Table S3 in ESI, the evolution of M_S with temperature is reported in Figure 6, and evolutions with the temperature of the two other parameters of the fit, b and $\chi_0(T)$ are reported in Figure S5 in ESI. The b parameter is usually of interest, in particular for nanoparticles, due to its link to the magnetic anisotropy constant K of the material, by $b = \beta\left(K/M_S\right)^2$, with β = 8/105 for cubic anisotropy or β = 4/15 for uniaxial anisotropy.[70,71] This relationship cannot be used here, unfortunately, in the absence of the composition and the crystallographic mass density of the actual material.

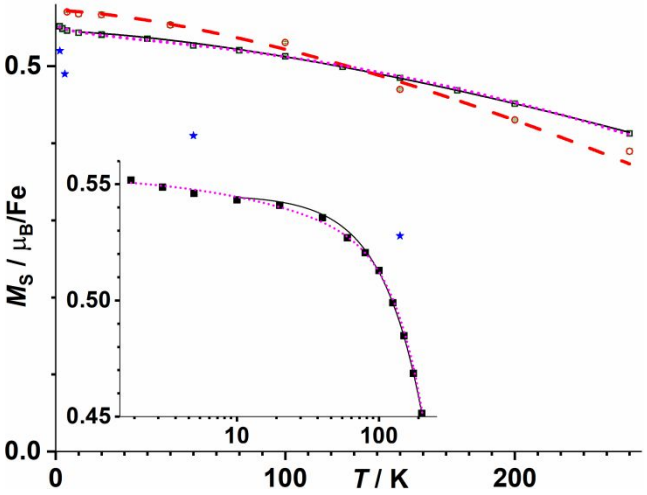

Figure 6. Evolution of the Fe(nP)/nC saturation magnetization M_S with temperature. M_S was obtained by fitting the 1st (black squares) and the 2nd (red circles) magnetometric measurements as described in the text. M_S obtained from XMCD spectra through sum rules application are also reported for comparison (blue stars, see the next section for details and discussion). Fits with the standard Bloch law are reported as black solid and red dashed lines, with the generalized Bloch law as magenta dotted line. Inset: close-up with the temperature in logarithmic scale.

We fitted the saturation magnetization M_S with the standard Bloch law (see ESI for full details, and the fit curves in Figure 6). For the 2nd measurement on the aged batch, the increase of M_S with decreasing temperature below 10 K led us to limit the fit to above that temperature. Overall values for the saturation magnetization did not change significantly over time: M_S/μ_B are 0.572(3) and 0.5484(8) per iron atom at 0 K respectively. At low temperatures, the observed upturn from the Bloch law $T^{3/2}$ behavior expected for the bulk has been previously reported for nanoscale ferromagnetic materials. Such an upturn has been explained to be due to defects induced by the nanostructuration, which permits Bose-Einstein condensation of magnons. The entropy contribution associated with this phenomenon introduces a correcting factor to the standard Bloch law.[72] A generalized Bloch law, derived analytically considering a Heisenberg spin model taking into account size, shape, and surface boundary conditions effects was proposed for ferromagnetic nanostructures.[73] Using that model (see full details in ESI) provided a more satisfactory fit of our data over the whole temperature range (R^2 increased from 0.9939 to 0.9985, see the magenta line on Figure 6 and inset), supporting size-effects induced by the scale of the nanocomposite.

The evolution with temperature of the remanent magnetization extracted from the hysteresis measurements is reported in Figure S6. For non-interacting particles, remanent magnetization is related to the distribution of anisotropy energy barriers:[59,66,67]

$$\frac{M_r(T)}{M_S(T)} = \frac{M_r(0)}{M_S(0)} \int_{T_B/\langle T_B \rangle}^{\infty} f(y)dy$$

where $y = T/\langle T_B \rangle$ is the reduced blocking temperature, $f(y)$ is the distribution of reduced blocking temperatures, and $M_r(0)/M_S(0)$ is the reduced remanence at 0 K. The latter is expected to be 0.5 in the Stoner-Wohlfarth model[7] for an assembly of independent particles with magnetic moment M_SV, uniaxial anisotropy and randomly oriented easy axes.[55,66] The variation of M_r with temperature was found to be roughly exponential (Figure S6). It should be mentioned that the temperature derivative of this reduced remanent magnetization is a direct measurement of the energy barrier distribution, and accordingly of blocking temperatures,[67] thus the derivative curves were fitted with a log-normal distribution (Figure S6). For both datasets, the $M_r(0)/M_S(0)$ factor was found to be indistinguishable from 0.5. The distributions of the T_B values were found to be centered at 45(7) K and 51(16) K respectively for the 1st and 2nd (*i.e.* on the aged sample) measurements. Considering those values as the average blocking temperatures,[59] they agree well with the previous values deduced from the ZFC measurement. The variation of the coercive field H_c with temperature (Figure S7) closely follows that observed for the remnant magnetization. Here three regimes are much more clearly observed, with evolutions of the form $H_c = H_{c0}\exp(-T/T_0)$, and crossover temperatures of about 60 and 200 K, and 20 and 170 K respectively for the 1st and 2nd measurements. While such an exponential dependence has been observed previously and accounted for by surface-to-core exchange coupling (exchange anisotropy),[55] this is not the temperature dependence expected for a uniform spin rotation.[7]

Curves of the thermal variation of the in-phase (m') and out-of-phase (m'') magnetic moments are reported in Figure S8. At 250 K, m'' is non-zero but appears to be frequency independent, while m' shows similar behavior to the ZFC curve but is frequency-dependent. Both components show frequency-dependent peaks, between 112 and 165 K for m' and 50 and 78 K for m'', which then decrease towards zero. With no evidence of strong inter-particle interactions, the frequency dependence is ascribed to the blocking process of the superparamagnetic nanoparticles and thus well-described by the Néel model.[7,57] The temperature dependence of the magnetization relaxation is expected to follow an Arrhenius law $\tau = \tau_0 exp\left(\langle K_{eff}\rangle\langle V\rangle/k_B T\right)$, with attempt time τ_0 expected in the 10^{-8} to 10^{-12} s range for isolated superparamagnetic nanoparticles.[70] Figure S8 reports the linear fit on the m'' maxima for different observation times $\tau_m = 1/2\pi\nu$, where ν is the frequency of the oscillating field (R^2 = 0.9872), yielding a slope of 1261(54) K and an intercept of 2.2×10^{-11} s. The fitted intercept τ_0 is in the expected range, while the slope yields $\langle K_{eff}\rangle = 1.5 \times 10^6$ Jm^{-3}, in perfect agreement with the value found from the ZFC curves.

X-ray Absorption Spectroscopy:

The samples were investigated by X-ray Absorption Spectroscopy (XAS) and X-ray Magnetic Circular Dichroism (XMCD) at the

DEIMOS beamline at the SOLEIL synchrotron light source (France)[74]. We used the element selectivity of the XAS technique to probe the nanocomposite properties at the $L_{2,3}$ absorption edges of Fe. We used here the highly sensitive Total Electron Yield (TEY) detection mode.[75] Because of its high sensitivity to site occupancy, XMCD can be used to unambiguously prove the presence of tetrahedrally coordinated ions in iron oxides or oxyhydroxides[76–78]. The XMCD signal can thus basically distinguish contributions from Fe(III) *versus* Fe(II) ions, Fe(III) ions on octahedral sites *versus* Fe(III) on tetrahedral sites, and Fe spin and orbit magnetic moments parallel *versus* antiparallel to the external magnetic field. In Figure 7, we report the XAS and XMCD measurements at 1.8, 4, 60 and 150 K under a 2 T saturation field, and the magnetization curves followed at the maximum of the XMCD signal. In the XAS and XMCD spectra, the observed peak and the respective peak profile are in good agreement with a tetrahedrally coordinated Fe(III).[76–78] In all the XMCD spectra in Figure 7, no small shoulder on the first negative peak of the dichroic signal at 708.0 eV is seen, thereby excluding the presence of Fe(II).[79] At the L_3- edge, according to previous multiplet theory calculations,[76,78] the positive peak labelled as A on Figure 7 left is ascribed to tetrahedral iron (T_h), while the two negative peaks labelled as B_1 and B_2 are ascribed to octahedral iron (O_h). At the L_2-edge, the peaks remain essentially positive, due to the competing influence of the T_h and O_h sites. One can use the ratio of the A to B_2 peaks, to discriminate between iron oxides/hydroxides phases. We report the ratios for the tested Fe(nP)/nC sample at the various measurement temperatures in Table S4.

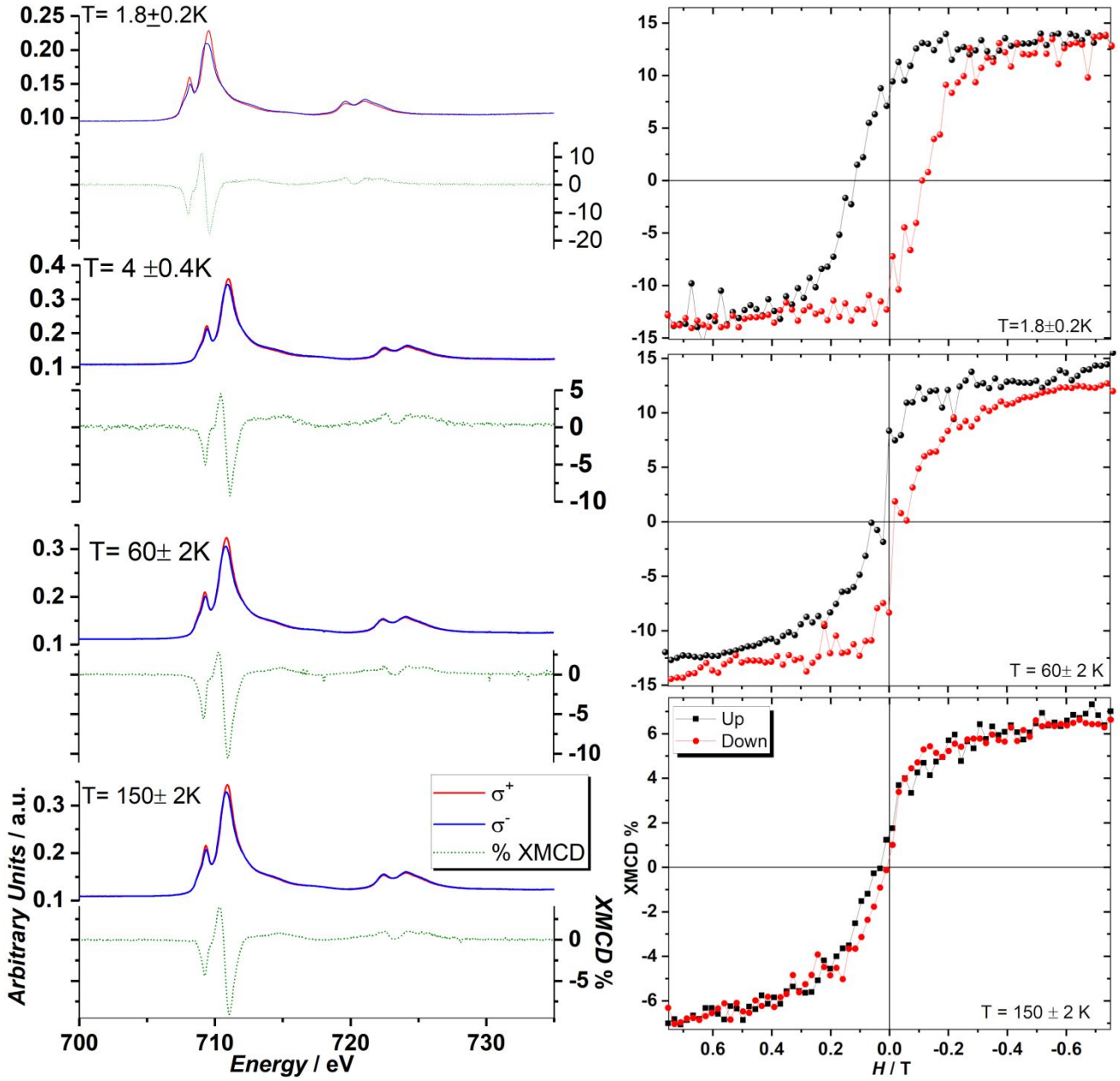

Figure 7. (left) XAS normalized spectra of Fe(nP)/nC at four different temperatures and relative XMCD spectra at $L_{2\text{-}3}$ edges; (right) XMCD detected magnetization curves for (n,k)=0° angle as a function of temperature in Fe(nP)/nC. These magnetization curves were measured in the same condition for all the samples (0.05 T s^{-1} scan speed).

The spin and orbital contributions to the magnetic moments of the cluster atoms can be separated, within the theoretical framework of the XMCD sum rules,[80–83] a quantitative analysis based on the integration of the XAS and XMCD spectra.[84] We obtained the orbital (m_L) and spin (m_S) magnetic moments on the Fe cations following the procedure detailed in ESI. Values obtained at temperatures of 1.8, 4, 60 and 150 K upon an applied magnetic field of 2 T in the direction parallel to the beam are reported in Table S5 in ESI.

We followed the sample magnetization by fixing the beam energy at the value at which the XMCD signal is maximal (see Figure 7). The magnetic hysteresis is clearly opened at 1.8 K. The coercive field at 1.8 K, at about 0.1 T, is remarkably larger than the one observed by magnetometry at the same temperature (37 mT). While decreasing, the hysteresis loop opening could still be observed up to 150 K. At higher temperatures the XMCD signal was too weak to be followed.

Relaxometry:

We completed the magnetic characterization of the nanocomposites with ^{1}H NMR relaxometry, performed at human body temperature (37°C), on a series of Fe(nP)/nC magnetic nanoflakes dispersed by strong sonication in water, with the help of a polymer dispersant, poly(acrylic acid) (PAA). The hydrodynamic diameters of the dispersions were measured by dynamic light scattering (DLS) in backscattering mode, well adapted to strongly light absorbing samples like graphene suspensions. The iron concentration of each sample was estimated by spectrophotometry (see Experimental section and Figure S12). Three suspensions were prepared with the following characteristics: [Fe]=0.67 mM (hydrodynamic diameter d_H=320 nm, polydispersity index by 2nd order Cumulant analysis PDI=0.26); [Fe]=0.40 mM (d_H=114 nm, PDI=0.278); [Fe]=0.17 mM (d_H=112 nm, PDI=0.225). Then the longitudinal and transverse nuclear proton relaxation times T_1 and T_2 at 60 MHz (1.41 T) of water molecules were measured at these three different equivalent iron concentrations (Figure 8). From the slopes of the plots of the relaxation rates R_1=1/T_1 and R_2=1/T_2 *versus* [Fe], we obtained a r_1 longitudinal relaxivity of 0.899(67) mM^{-1}s^{-1}, and a r_2 transverse relaxivity of 24.94(14) mM^{-1}s^{-1}, which will be discussed within the framework of the accepted inner and outer sphere models of (super)paramagnetic contrast agents for MRI.

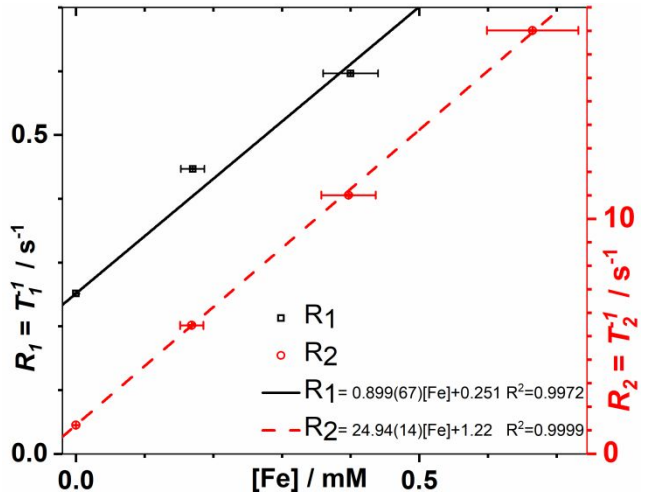

Figure 8. Proton relaxation rates: plot of R_1=1/T_1 (black squares) and R_2=1/T_2 (red circles), and corresponding linear fits, against the equivalent iron concentration in several Fe(nP)/nC aqueous dispersions, measured under 1.41 T (60 MHz) at 37°C. Vertical errors bars were derived directly from measurements, concentration errors were estimated at ±10% as determined from the spectrophotometric method described in ESI in Figure S14.

Discussion:

The Fe(nP)/nC nanocomposite acts as a quite soft magnet since magnetization above 1 T is seen to increase almost linearly with the field. In general, this may be related to a contribution from either *i)* paramagnetic impurities, *ii)* the smaller particles remaining in the superparamagnetic regime, *iii)* non-collinear arrangement of atomic spins that may be observed in core-shell nanoparticle structures with significant differences between the surface and the core, leading to disordered spin configurations and thus a reduced magnetic moment.[85] The ZFC curve above T_{max} flattens in a plateau until converging with the FC curve at T_{irr}. The very large difference between T_{max} and T_{irr} would usually point towards a huge spread in particle size distribution, in particular since other systems of similar size show smaller temperature differences.[57–60] Nevertheless, this interpretation is not compatible with the narrow size distribution evidenced by TEM and the powder XRD data, where only broad peaks are observed on the pristine material. Such features exclude the presence of crystalline domains of size above a few nm, which would provide more defined diffraction peaks.

The T_{max}-T_{irr} spread as an estimate of the particle size distribution relies on the assumption of a lack of inter-particle interactions and similar anisotropy constants.[59,85] Concerning inter-particle interactions, a qualitative indication is found in the Field-Cooled magnetization curve, where the continuous decrease with increasing temperature is a qualitative indication that indeed whatever magnetic inter-particle interactions should be quite weak, as pointed out in the literature.[59] Thus we propose that the discrepancy observed in the T_{max}-T_{irr} spread be linked to a wide distribution of anisotropy constants for the nanocomposites, from differences in size, shape, and/or composition.

This interpretation is corroborated by the measured Mössbauer spectrum showing a quadrupolar doublet, and a major magnetically ordered component that can be explained as an assembly of magnetic nanoparticles, with superparamagnetic relaxation times that are respectively shorter or longer than the characteristic time scale of Mössbauer scattering (~5 ns).[59] For non-interacting particles, the $f(y)$ distribution intervening in the remanent magnetization formula (see above) should reflect the underlying distribution of particle volumes. If any dependence of the anisotropy constant with either size or temperature is neglected, then the widths of the $f(y)$ log-normal distributions should be close to 3 times that for the particles' diameters ($3\times\sigma_{TEM}$ = 0.3). The values of 1.4(1) and 1.7(2) for the 1st and 2nd measurements respectively, would indicate nanoparticles that are even smaller than suggested by TEM analysis. This may be related to the tendency to overlook the population of smaller objects in electron microscopy as compared to their average contribution to the magnetic properties.

M_S saturation magnetization values fall well in the range of ferrimagnetic oxides, which show values in the bulk about 1.27-1.38 μ_B/Fe for Fe_3O_4 (corresponding to the S=2 moment of Fe^{2+} in the O_h sites, the moments of the S=5/2 Fe^{3+} cations being antiferromagnetically coupled between the T_d and O_h sites of the inverse spinel), 0.86-1.14 μ_B/Fe (γ-Fe_2O_3) or 0.11-0.32 μ_B/Fe (δ-FeOOH). Meanwhile M_S values for nanoparticles are known to be significantly lower, as shown for examples on some Fe_3O_4@γ-Fe_2O core-shell examples.[56] Values for the effective anisotropy constants are consistent across the various measurements. Most importantly

they are in line with the higher values usually observed in nanoparticles, one or two order of magnitude above bulk values. This is attributed to the larger magnetic anisotropy contribution coming from the surface ions, caused by the loss of symmetry,[86] which leads to a dependence as a function of diameter in $1/<D>$.[87] The Curie temperatures resulting from the fits are well above room temperature and show some increase between measurements. While obtaining reliable values would require measurements at higher temperatures, which would lead to irreversible changes in the nanocomposite, it is nevertheless remarkable that, as expected for nanoparticles, they are about midway towards the high values reported for bulk potassium ferrites: 960 K for KFeO2,[13] about 780 K for $KFe_{11}O_{17}$,[20] and 713 K for $K_{1.33}Fe_{11}O_{17}$.[21] Concerning the small rise observed at low temperature for the second measurement, while magnetic impurities would be a ready explanation, the $\chi_0(T)$ evolution with temperature shows in Figure S5 a rather linear and flat behavior for both measurements, which does not support that explanation.

As reported in the literature, the shape and energy positions of the XMCD spectra labelled A, B_1 and B_2 (see Figure 7) are similar to Fe_2O_3 nanoparticles.[76–78] The A/B_2 ratio is very useful to discriminate between iron oxides/hydroxides phases, suggesting a lower amount of tetrahedral iron compared to the values reported for 1-line or 2-lines ferrihydrite and maghemite.[76,78,88,89] Unfortunately, direct comparison with potassium ferrites was not possible since XMCD spectra have not been reported in the literature so far. Table S4 illustrates that Fe(nP)/nC composites are somewhere in between ferrihydrite and maghemite from a structural point of view. For direct comparison with magnetometry, we also plotted M_S values in Figure 6. M_S values found by XMCD, a local probe, appear to be in good agreement with values derived from standard bulk magnetometry measurements, especially at low temperatures, resulting in nice corroboration to calculations. As seen in Table S5, orbital moments are negligible, as expected for Fe(III). This fact combined with the overall difference in line shape does not support the presence of Fe(II) such as FeO (see Figure S9). Instead, it suggests that the magnetic contribution comes almost entirely from the Fe(III) centers, which are present as a mixed oxo-hydroxoferrate phase. Since the Fe 2p and 3p photoemission peaks strongly indicate that only Fe(III) is present in Fe(nP)/nC, amongst the phases we mentioned previously, we narrowed the possible phases present in this sample to either $K_2Fe_4O_7$, or the mixed oxo-hydroxoferrate phase $K_{2-x}Fe_4O_{7-x}(OH)_x$. As stated above, those phases are usually formed at high temperatures,[10] so the formation of similar phases here appears rather surprising given the mild reaction conditions of wet chemistry. Isomeric shifts values for potassium ferrites tetrahedral sites are usually closer to zero (in KFeO2,[13,90] $K_6Fe_2O_6$,[12] $K_2Fe_4O_7$,[17] $K_{2-x}Fe_4O_{7-x}$,[19] $K_{1+x}Fe_{11}O_{17}$[91]), while barium-potassium ferrites[92] or cobalt ferrites[59] lead to values similar to what has been observed here, about 0.4 mm/s. XRD measurements performed on the TGA residue, XPS and ICP data, supports the assertion that potassium is incorporated in the nanoparticle crystal structure.

The transverse relaxivity r_2 value is in line with those reported on other ultrasmall nanoparticles: 4 nm sugar coated Fe_3O_4 (r_1/r_2 23/28 $mM^{-1}s^{-1}$),[57] 2.2 and 3 nm γ-Fe_2O_3 (4.78/17.5 and 4.77/29.2 $mM^{-1}s^{-1}$ respectively under 3 T),[93] 6 nm iron oxide mnPs coated with PEG (7.3/17.5 $mM^{-1}s^{-1}$ under 1.41 T),[94] 8.3 nm iron oxide mnPs coated with glycopeptides (16/62 $mM^{-1}s^{-1}$ under 1.5 T),[95] 3.3 nm iron oxide (8.3/35.1 $mM^{-1}s^{-1}$ under 4.7 T),[96] 3 nm manganese ferrite (2.6(3)/7.4(9) $mM^{-1}s^{-1}$),[97] 2.2-2.6 nm manganese ferrite (6.61/35.92 $mM^{-1}s^{-1}$ under 4.7 T),[60] 2 and 3 nm ferrite (8.43/21.02 and 8.23/21.97 $mM^{-1}s^{-1}$ respectively under 3 T),[98] and PEG polymer coated 3 nm $MnFe_2O_4$ mnPs (8.26-10.21/21.27-38.64 $mM^{-1}s^{-1}$ under 3 T).[99] Meanwhile the longitudinal relaxivity r_1 is definitely smaller, which likely reflects that the nanoparticle surface is not very accessible to water molecules for direct complexation ("inner sphere" mechanism), and with the graphene flake also likely causing steric hindrance of the diffusion of the water molecules around the magnetic center ("outer sphere" mechanism), a mechanism already reported for the slower water dynamics in hydrophobic pockets of proteins.[100] A similar decrease of r_1 was reported when 4 nm diameter mnPs were inserted in the hydrophobic environment of polymer vesicle membranes as compared to the initial mnPs freely floating in water.[101] As a result, their very high r_2/r_1 ratio around 27.7 make the Fe(nP)/nC ideal contrast agents for T_2- or T_2*-weighted MRI imaging sequences.

Conclusions: Through a combination of chemical characterization, microscopy, magnetometry, Mössbauer, X-ray photoemission and absorption spectroscopies, we determined that the nanocomposite material obtained by mild water oxidation of the reaction product between potassium graphenide and an Fe(II) salt consists of ultrasmall potassium ferrite nanoparticles, still grafted to the graphene nanoflakes. The generated nanoparticles are most likely a mixture between $K_2Fe_4O_7$, and $K_{2-x}Fe_4O_{7-x}(OH)_x$. The magnetic properties as evidenced by magnetometry and X-ray Magnetic Circular Dichroism are widely different from classical ultrasmall iron oxide nanoparticles, which are known in literature to invariably display superparamagnetic behavior. This is indeed in sharp contrast with the slightly hysteretic magnetization curves (*i.e.* exhibiting non-zero remanence and coercivity) at temperatures close to ambient conditions that we observed for the nanocomposite material. The huge value obtained for the effective magnetic anisotropy K_{eff}, extracted with converging values from two different approaches, XMCD and classical magnetic characterization, accounts for the presence of magnetic ordering at rather high temperatures. The synthesis of ultrasmall potassium ferrite nanoparticles in such mild conditions is unexpected given the harsh conditions used for classical syntheses of bulk potassium ferrites and is of utmost relevance. Moreover, due to the simplicity of the reaction protocol, this synthetic pathway may be translated directly to analogous reactions, showing the synthetic value of this study. This detailed study also demonstrated the need of carefully conducted identification of the generated nanoparticle phase, especially involving templated nanoparticles on substrates like in this case, where careful analysis of rather poorly ordered crystalline nanoparticle phases is only possible by applying a wide array of different physical and chemical characterization tools. These findings also shed a new light on the electrocatalytic properties of those nanocomposite materials,[39] considering that potassium ferrites are used in all sorts of catalytic processes and as solid state electrolytes due to their transport properties,[11,18,19,23–28] with possibly a synergistic interaction between the conductive carbon layers with the electronic states of the potassium ferrite nanoparticles. Therefore, electrochemical characterization, especially in the context of the oxygen evolution or reduction reaction, may offer further insights into this fascinating interaction. Finally, the proton NMR relaxometric study showed an unusual behavior of these magnetic nanocomposite: unlike most ultra-small superparamagnetic iron oxide nanoparticles of core diameter around 3 nm which behave as positive MRI contrast agents when well-dispersed by a hydrophilic repulsive coating (thanks to large longitudinal relaxivity r_1 and moderate r_2/r_1 ratio, typically below 3-4),[102] the magnetic nanocomposite here exhibits low r_1=0.86 $mM^{-1}s^{-1}$ and high r_2/r_1 ratio of 28 at 1.41 T (clinically relevant field). This behavior is interpreted by the binding of the magnetic center to the large and hydrophobic graphene flake, which impedes the inner sphere mechanism of proton longitudinal relaxation (by avoiding direct contact with water molecules) while promoting the outer sphere mechanism to transverse relaxation (*i.e.* fluctuating magnetic dipolar interaction at long distance between the nuclear

spins of water and the high electronic moments of the Fe(nP) magnetic cores). Thus monitoring the distribution of Fe(nP)/nC composite by T_2-weighted MRI sequence is feasible for biomedical applications such as magnetic drug nanocarriers, after their proper functionalization by a repelling shell of biocompatible macromolecules for *in vivo* injection.

Experimental Section: XPS: XPS spectra were measured in an ultra-high vacuum ThermoFisher K-Alpha photoelectron spectrometer. XPS characterization was performed with a microfocused monochromatic Al Kα radiation source (h_v = 1486.7 eV), spectra were recorded in normal emission, with α_{out} = 0° with respect to the surface normal. The hemispherical electron energy analyzer was operated in the constant analyzer energy mode at an analyzer pass energy of Ep =40 eV (survey spectra) and Ep = 10 eV (high-resolution detailed spectra). The samples were investigated without any UHV pre-treatment. The binding energies (BE) of all the spectra were referenced to a BE of 284.2 eV for the C1s line as the main feature of the carbon tape used as conducting substrate. Datasets were treated with the CASA-XPS software. Shirley functions were used to subtract the background, and the peaks were then deconvoluted with the Gupta and Sen multiplet structure corresponding to Fe(III).[62–64]

ICP-OES: For microanalysis, about 0.5-1.5 mg of sample was weighed accurately in Säntis light tin capsules for solids with a Mettler MX5 microbalance. The capsules were digested with a 1:1 mixture of 70% nitric acid (3 mL) and 98% sulfuric acid (3 mL) in a Schott flask, refluxing at 135°C until complete dissolution was observed (between 3h and overnight). The resulting solution was then diluted by addition of milliQ water to 20 mL. TGA residues were weighed on pieces of aluminum foil and transferred to a Schott flask, digested with a 1:1 mixture of 70% HNO_3 (3 mL) and 37% HCl (3 mL), at 90°C overnight, then diluted with milliQ water to 50 mL. Fe, B and K contents were then quantified with a Varian ES-720 ICP-OES. Empty tin capsules showed no relevant content for those elements.

Powder X-ray Diffraction: Powder X-ray diffraction data were recorded using a PANalytical X'Pert MPD PRO diffractometer with Bragg-Brentano geometry, Cu Kα radiation (λ = 1.54184 Å) and a secondary graphite 370 monochromator. Considering the very small amount of sample, it was measured on a zero background silicon wafer sample holder from PANalytical, on a 8-80° 2θ angular range over 13920s. Data were analyzed with Jana2006 software.[103]

TEM: TEM measurements were performed on a TEM-FEG HR (JEOL 2200FS). TEM grids were prepared by drop casting 20 µL of nanocomposite dispersion in THF, sonicated in a bath sonicator for 10 min, directly onto SF400-CU (silicon monoxide membranes on 400 mesh copper grid, (Electron microscopy science)). The grid was dried at room temperature and used without further purification.

Mössbauer spectroscopy characterization: A few milligrams of sample was encapsulated in Mylar and ^{57}Fe transmission Mössbauer spectra were recorded in transmission geometry using a constant acceleration Halder–type spectrometer with a room temperature ^{57}Co source (embedded in Rh matrix). The velocity scale was calibrated according to the ^{57}Fe Mössbauer spectrum of a pure α-Fe(0) foil recorded at room temperature. A helium bath cryostat suitable for Mössbauer experiments was used in order to record spectra from room temperature down to 4.2 K. The Mössbauer hyperfine parameters (δ isomer shift, Δ quadrupole splitting, 2ε quadrupole shift, B_{hf} hyperfine magnetic field, Γ Lorentzian linewidth and relative areas) were refined using both homemade programs and the WinNormos® software (Wissenschaftliche Elektronik GmbH). When distributions of the quadrupole splitting or hyperfine magnetic field parameter were considered, their mean value (*) and standard deviation are reported in the table of hyperfine parameters.

Magnetic characterization: Magnetic measurements were performed on a Quantum Design MPMS-7XL SQUID and a Microsense EZ-7 Vibrating Sample magnetometers. The MPMS-7XL was used with both DC and the Reciprocating Sample options. Samples were weighed accurately with a Mettler MX5 microbalance. SQUID samples were sealed in 30 µm-thick polyethylene bags, while VSM samples were enclosed in Säntis light tin capsules for solids. For the main sample presented here, the VSM sample was prepared using the sample previously measured at low temperature in the MPMS-7XL. Diamagnetic contributions of the sample holders had been determined separately and were accordingly subtracted from the measurements. Magnetization values were normalized respective to the Fe cation content as determined by the ICP analysis. Zero Field Cooled/Field Cooled experiments were performed by cooling the sample under zero and 1T magnetic field respectively, then measuring with increasing temperature under a 5 mT field. ac susceptibility was measured under zero dc field with a 0.38 mT oscillating field between 0.1 and 512 Hz. Isothermal magnetization curves could not be rigorously corrected for the sample demagnetizing field, the exact shape, composition and density of the nanoparticles being unknown. Nevertheless, assuming that the nanoparticles were composed of the $K_2Fe_4O_7$ phase (413.57 g mol^{-1}, density of 4323.5 kg m^{-3}), of spherical shape with a 2.8nm diameter, the correction was seen to be small (Figure S11 in Supporting Information) and was thus neglected. Measurements on another batch of nanocomposite provided similar results.

XAS characterization: XAS and XMCD characterizations were performed at the DEIMOS beamline of the SOLEIL synchrotron facility (France) on a sample of disperse NP-flakes on a Au polycrystalline substrate. The UHV compatible pumped ^{4}He optical cryomagnet of the beamline was used and absorption spectra were measured in total electron yield (TEY) detection mode to guarantee optimal detection sensitivity. All the characterizations were performed using a low photon density to avoid radiation damages. XMCD spectra were obtained placing the normal of sample surface at 0° with respect to the X-ray light propagation vector and extracted as ($\sigma_L - \sigma_R$). The final XMCD spectrum is the result of the averaging of four scans per polarization, for both positive and negative magnetic field in order to avoid contamination from spurious X-ray Magnetic Linear Dichroism (XMLD). The spectra were measured at temperatures of 1.8, 4, 60 and 150 K and under an applied magnetic field of 2 T parallel to the X-ray propagation vector. The same setup was used to record the XMCD dependence on the magnetic field (hysteresis curves) as a function of sample temperature, as well as field sweeping rate. Data were normalized with respect to the saturation value in order to be able to compare this experiment with traditional magnetometry experiments. Again, measurements on another batch of nanocomposite provided similar results.

Proton NMR relaxometry: Water dispersions of Fe(nP)/nC nanocomposites were obtained by weighing between 0.2 and 2 mg of powder in 0.1-1 mL of 1 wt.% solution of stabilizing polymer (poly(acrylic acid), sodium salt, M_n~5100 g·mol^{-1}, Sigma-Aldrich, L'Isle-d'Abeau, France). The pH was adjusted near 7 using a solution of NaOH 0.01 mol·L^{-1}. Suspensions were sonicated for 20 min at 75% power (3" pulse On, 2" pulse off) with a tip ultrasonic processor (Sonics 130 W Vibracell, Thermofisher Scientific, France) and then filtered with a 0.45 µm pore size membrane to remove remaining aggregates. The iron concentration was evaluated using a non-destructive method consisting in acquiring the full UV-Vis absorption spectrum in a quartz cuvette between

250 and 850 nm and comparing it to a calibration curve obtained by Inductively Coupled Plasma Atomic Emission Spectroscopy (ICP-AES) for suspensions of maghemite nanoparticles, which was shown to be independent of their diameters,[104] see Figure S12. The proper dispersion state of the suspensions was checked by dynamic light scattering with a remote head DLS setup (Vasco™ Flex, Cordouan Technologies, Pessac, France). Finally, 0.7 mL of each suspension was placed in a tube pre-heated at 37°C with a thermostatic bath before measuring their longitudinal (T_1) and transverse (T_2) proton relaxation times with a Bruker minispec mq60 relaxometer with a 1.41 T magnet (60 MHz proton resonance), using respectively inversion-recovery (IR) and Carr-Purcell-Meiboom-Gill (CPMG) spin-echo sequences. Receiver gain, repetition time (TR), echo time (TE), number of data points per curve (typically 20 for IR sequence and 200 for CPMG) and recycling delay (RD) were adjusted carefully using criteria to optimize the signal-to-noise ratio and minimize the experimental uncertainty on the measured T_1 and T_2 values.[105] The decay rates defined as $R_1=1/T_1$ and $R_2=1/T_2$ were plotted as a function of [Fe] and fitted by linear regression, imposing the intercepts with [Fe]=0 mM to the values measured for pure water: $R_1°= 0.25\ s^{-1}$ and $R_2°= 1.22\ s^{-1}$. Longitudinal (r_1) and transverse (r_2) relaxivities were determined as the experimental slopes of these two plots (see Figure 8).

ASSOCIATED CONTENT

Supporting Information

The ESI contains, further analysis, analysis details (Bloch law), and further detail and physicochemical characterization such as XPS, Mössbauer, XRD, ICP-OES, UV-Vis and DLS, as well as further details to the XAS and XMCD measurements.
The Supporting Information, pdf file, is available free of charge on the ACS Publications website.

AUTHOR INFORMATION

Corresponding Authors

patrick.rosa@icmcb.cnrs.fr and ferdinand.hof@u-bordeaux.fr

Author Contributions

FH, PR and AP contributed to conceptualization, FH, LP, MD, PR, OS to data acquisition & analysis, all authors to investigation, AP to project administration, FH, LP, PR to visualization and writing original draft, all authors to writing, review and editing.

Notes

The authors declare no competing financial interests.

ACKNOWLEDGMENT

This work was supported by CNRS (Momentum project 2017, FH) and the French National Research Agency (ANR) Investment for the Future Programme IdEx Bordeaux (ANR-10-IDEX-03-02, MG and LP). Financial support from the CPER CAMPUSB project funded by the French state and the New Aquitaine region is gratefully acknowledged for acquisition of the Bruker Minispec™ mq60 relaxometer (LCPO and ICMCB). The SOLEIL synchrotron light source is acknowledged for providing access to the DEIMOS beamline (proposals 20161074 and 9950071). We also acknowledge all the ICMCB and CRPP staff for their support with the measurements, and E. Hillard for manuscript proofreading.

REFERENCES

(1) Ulbrich, K.; Holá, K.; Šubr, V.; Bakandritsos, A.; Tuček, J.; Zbořil, R. Targeted Drug Delivery with Polymers and Magnetic Nanoparticles: Covalent and Noncovalent Approaches, Release Control, and Clinical Studies. *Chem. Rev.* **2016**, *116* (9), 5338–5431. https://doi.org/10.1021/acs.chemrev.5b00589.

(2) Frey, N. A.; Peng, S.; Cheng, K.; Sun, S. Magnetic Nanoparticles: Synthesis, Functionalization, and Applications in Bioimaging and Magnetic Energy Storage. *Chem. Soc. Rev.* **2009**, *38* (9), 2532–2542. https://doi.org/10.1039/b815548h.

(3) Lu, A. H.; Salabas, E. L.; Schüth, F. Magnetic Nanoparticles: Synthesis, Protection, Functionalization, and Application. *Angew. Chemie - Int. Ed.* **2007**, *46* (8), 1222–1244. https://doi.org/10.1002/anie.200602866.

(4) Lu, A. H.; Schmidt, W.; Matoussevitch, N.; Bönnemann, H.; Spliethoff, B.; Tesche, B.; Bill, E.; Kiefer, W.; Schüth, F. Nanoengineering of a Magnetically Separable Hydrogenation Catalyst. *Angew. Chemie - Int. Ed.* **2004**, *43* (33), 4303–4306. https://doi.org/10.1002/anie.200454222.

(5) Gao, J.; Gu, H.; Xu, B. Multifunctional Magnetic Nanoparticles: Design, Synthesis, and Biomedical Applications. *Acc. Chem. Res.* **2009**, *42* (8), 1097–1107. https://doi.org/10.1021/ar9000026.

(6) Batlle, X.; Labarta, A. Finite-Size Effects in Fine Particles: Magnetic and Transport Properties. *J. Phys. D. Appl. Phys.* **2002**, *35* (6), R15–R42. https://doi.org/10.1088/0022-3727/35/6/201.

(7) Dormann, J. L.; Fiorani, D.; Tronc, E. MAGNETIC RELAXATION IN FINE-PARTICLE SYSTEMS. In *Advances in Chemical Physics*; Prigogine, I., Rice, S. A., Eds.; John Wiley & Sons, Inc, 1997; Vol. 98, pp 283–494.

(8) Wu, L.; Mendoza-Garcia, A.; Li, Q.; Sun, S. Organic Phase Syntheses of Magnetic Nanoparticles and Their Applications. *Chem. Rev.* **2016**, *116* (18), 10473–10512. https://doi.org/10.1021/acs.chemrev.5b00687.

(9) Cornell, R. M.; Schwertmann, U. *The Iron Oxides*; WILEY-VCH Verlag GmbH & Co. KGaA: Weinheim, 2003.

(10) Shaikhutdinov, S. K.; Weiss, W.; Schlögl, R. Interaction of Potassium with Fe3O4(111) at Elevated Temperatures. *Appl. Surf. Sci.* **2000**, *161* (3), 497–507. https://doi.org/10.1016/S0169-4332(00)00373-1.

(11) Joseph, Y.; Ketteler, G.; Kuhrs, C.; Ranke, W.; Weiss, W.; Schlögl, R. On the Preparation and Composition of Potassium Promoted Iron Oxide Model Catalyst Films. *Phys. Chem. Chem. Phys.* **2001**, *3* (18), 4141–4153. https://doi.org/10.1039/b104263g.

(12) Sharma, V. K.; Machala, L. Mechanism of Thermal Decomposition of K2FeO4 and BaFeO4: A Review. *Hyperfine Interact.* **2016**, *237* (1), 1–8. https://doi.org/10.1007/s10751-016-1338-x.

(13) Tomkowicz, Z.; Szytuka, A. Crystal and Magnetic Structure of KFeO2. *J. Phys. Chem. Solids* **1977**, *38*, 1117–1123. https://doi.org/10.1016/0022-3697(77)90037-3.

(14) Möller, A. Das Gemischtvalente Ternäre Oxoferrat(II,III) K3[Fe2O4] – Eine Aufgefüllte Variante Des K2[Fe2O4]-Typs. *Zeitschrift für Anorg. und Allg. Chemie* **2001**, *627* (11), 2537. https://doi.org/10.1002/1521-3749(200111)627:11<2537::AID-ZAAC2537>3.0.CO;2-G.

(15) Rieck, H.; Hoppe, R. The First Oxoferrate(III) Having a Discrete Anion: K6[Fe2O6]. *Angew. Chemie Int. Ed. English* **1973**, *12* (8), 673–674. https://doi.org/10.1002/anie.197306731.

(16) Müller, H.-P.; Hoppe, R. Das Erste Oligomere Oxoferrat(III): K14[Fe4O13]. *Zeitschrift für Anorg. und Allg. Chemie* **1990**, *580* (1), 57–70. https://doi.org/10.1002/zaac.19905800108.

(17) Vinš, J.; Urbanová, M.; Šubrt, J.; Zapletal, V.; Zakharov, A. A.; Shaplygin, I. S. Reaction of α-Fe2O3 (Hematite) with Potassium Carbonate at Elevated Temperatures. *Collect. Czechoslov. Chem. Commun.* **1986**, *51* (4), 809–818. https://doi.org/10.1135/cccc19860809.

(18) Ito, S.; Kurosawa, H.; Akashi, K.; Michiue, Y.; Watanabe, M. Crystal Structure and Electric Conductivity of K+-$beta;-Ferrite with Ideal Composition KFe11O17. *Solid State Ionics* **1996**, *86–88*, 745–750. https://doi.org/10.1016/0167-2738(96)00164-6.

(19) Albrecht, R.; Hunger, J.; Block, T.; Pöttgen, R.; Senyshyn, A.; Doert, T.; Ruck, M. Oxo-Hydroxoferrate K2−xFe4O7−x(OH)x: Hydroflux Synthesis, Chemical and Thermal Instability, Crystal and Magnetic Structures. *ChemistryOpen* **2019**, *8* (1), 74–83. https://doi.org/10.1002/open.201800229.

(20) Gorter, E. W. Interactions in Various Magnetic Compounds. *J. Appl. Phys.* **1963**, *34* (4), 1253–1259.

https://doi.org/10.1063/1.1729460.
(21) Edström, K.; Ito, S.; Delaplane, R. G. Crystal and Magnetic Structure of Nonstoichiometric K+β-Ferrite. *J. Magn. Magn. Mater.* **2000**, *212* (3), 347–354. https://doi.org/10.1016/S0304-8853(99)00831-8.
(22) Khanna, L.; Verma, N. K. Synthesis, Characterization and Biocompatibility of Potassium Ferrite Nanoparticles. *J. Mater. Sci. Technol.* **2014**, *30* (1), 30–36. https://doi.org/10.1016/j.jmst.2013.10.008.
(23) Zhang, X.; Geng, Z.; Jian, J.; He, Y.; Lv, Z.; Liu, X.; Yuan, H. Potassium Ferrite as Heterogeneous Photo-Fenton Catalyst for Highly Efficient Dye Degradation. *Catalysts* **2020**, *10* (3), 293. https://doi.org/10.3390/catal10030293.
(24) Toledo, J.; García, X.; Gordon, A. L.; Jiménez, R. Magnesia-Supported Potassium Oxide Catalysts for Soot Combustion: Effect of Fe Addition on the Catalyst Activity and Stability. *React. Kinet. Mech. Catal.* **2014**, *113* (2), 487–497. https://doi.org/10.1007/s11144-014-0758-3.
(25) Dudley, G. J.; Steele, B. C. H.; Howe, A. T. Studies of Potassium Ferrite K1+xFe11O17. I. Electronic Conductivity and Defect Structure. *J. Solid State Chem.* **1976**, *18* (2), 141–147. https://doi.org/10.1016/0022-4596(76)90088-8.
(26) Dudley, G. J.; Steele, B. C. H. Studies of Potassium Ferrite K1+xFe11O17. III. Ionic Conductivity and Chemical Diffusion. *J. Solid State Chem.* **1977**, *21* (1), 1–12. https://doi.org/10.1016/0022-4596(77)90138-4.
(27) Yuan, H.; Li, H.; Zhang, T.; Li, G.; He, T.; Du, F.; Feng, S. A K2Fe4O7 Superionic Conductor for All-Solid-State Potassium Metal Batteries. *J. Mater. Chem. A* **2018**, *6* (18), 8413–8418. https://doi.org/10.1039/c8ta01418c.
(28) Ito, S.; Washio, M.; Makino, I.; Koura, N.; Akashi, K. Role of Potassium Ions in Humidity Sensitivity of K+-β-Ferrite. *Solid State Ionics* **1996**, *86–88*, 1005–1011. https://doi.org/10.1016/0167-2738(96)00242-1.
(29) Zhang, B.; Yu, Q.; Liu, Y. Alternating Magnetic Field Controlled Targeted Drug Delivery Based on Graphene Oxide-Grafted Nanosupramolecules. *Chem. – A Eur. J.* **2020**, *26* (60), 13698–13703. https://doi.org/10.1002/chem.202003328.
(30) Singh, N.; Ansari, J. R.; Pal, M.; Thanh, N. T. K.; Le, T.; Datta, A. Synthesis and Magnetic Properties of Stable Cobalt Nanoparticles Decorated Reduced Graphene Oxide Sheets in the Aqueous Medium. *J. Mater. Sci. Mater. Electron.* **2020**, *31* (18), 15108–15117. https://doi.org/10.1007/s10854-020-04075-2.
(31) Lin, C.-H.; Chen, Y.-C.; Huang, P.-I. Preparation of Multifunctional Dopamine-Coated Zerovalent Iron/Reduced Graphene Oxide for Targeted Phototheragnosis in Breast Cancer. *Nanomaterials* **2020**, *10* (10), 1957. https://doi.org/10.3390/nano10101957.
(32) Bai, L.-Z.; Zhao, D.-L.; Xu, Y.; Zhang, J.-M.; Gao, Y.-L.; Zhao, L.-Y.; Tang, J.-T. Inductive Heating Property of Graphene Oxide–Fe3O4 Nanoparticles Hybrid in an AC Magnetic Field for Localized Hyperthermia. *Mater. Lett.* **2012**, *68*, 399–401. https://doi.org/10.1016/j.matlet.2011.11.013.
(33) Lerra, L.; Farfalla, A.; Sanz, B.; Cirillo, G.; Vittorio, O.; Voli, F.; Le Grand, M.; Curcio, M.; Nicoletta, F.; Dubrovska, A.; Hampel, S.; Iemma, F.; Goya, G. Graphene Oxide Functional Nanohybrids with Magnetic Nanoparticles for Improved Vectorization of Doxorubicin to Neuroblastoma Cells. *Pharmaceutics* **2018**, *11* (1), 3. https://doi.org/10.3390/pharmaceutics11010003.
(34) Wang, F. H.; Bae, K.; Huang, Z. W.; Xue, J. M. Two-Photon Graphene Quantum Dot Modified Gd 2 O 3 Nanocomposites as a Dual-Mode MRI Contrast Agent and Cell Labelling Agent. *Nanoscale* **2018**, *10* (12), 5642–5649. https://doi.org/10.1039/C7NR08068A.
(35) Wang, G.; Chen, G.; Wei, Z.; Dong, X.; Qi, M. Multifunctional Fe3O4/Graphene Oxide Nanocomposites for Magnetic Resonance Imaging and Drug Delivery. *Mater. Chem. Phys.* **2013**, *141* (2–3), 997–1004. https://doi.org/10.1016/j.matchemphys.2013.06.054.
(36) Idisi, D. O.; Oke, J. A.; Sarma, S.; Moloi, S. J.; Ray, S. C.; Pong, W. F.; Strydom, A. M. Tuning of Electronic and Magnetic Properties of Multifunctional R-GO-ATA-Fe 2 O 3 -Composites for Magnetic Resonance Imaging (MRI) Contrast Agent. *J. Appl. Phys.* **2019**, *126* (3), 035301. https://doi.org/10.1063/1.5099892.
(37) Hof, F.; Kampioti, K.; Huang, K.; Jaillet, C.; Derré, A.; Poulin, P.; Yusof, H.; White, T.; Koziol, K.; Paukner, C.; Pénicaud, A. Conductive Inks of Graphitic Nanoparticles from a Sustainable Carbon Feedstock. *Carbon N. Y.* **2017**, *111*, 142–149. https://doi.org/10.1016/j.carbon.2016.09.052.
(38) Gustavo Cançado, L.; Gomes da Silva, M.; Martins Ferreira, E. H.; Hof, F.; Kampioti, K.; Huang, K.; Pénicaud, A.; Alberto Achete, C.; Capaz, R. B.; Jorio, A. Disentangling Contributions of Point and Line Defects in the Raman Spectra of Graphene-Related Materials. *2D Mater.* **2017**, *4* (2), 025039. https://doi.org/10.1088/2053-1583/aa5e77.
(39) Hof, F.; Boni, A.; Valenti, G.; Huang, K.; Paolucci, F.; Penicaud, A. From Food Waste to Efficient Bifunctional Nonprecious Electrocatalyst. *Chem. - A Eur. J.* **2017**, *23* (61), 15283–15288. https://doi.org/10.1002/chem.201704041.
(40) Hof, F.; Penicaud, A. Graphenide Solutions: A Chemical Platform for Nanoparticle Nanocarbon Composites. *Chem. - A Eur. J.* **2018**, 1–12. https://doi.org/10.1002/chem.201801694.
(41) Catheline, A.; Vallés, C.; Drummond, C.; Ortolani, L.; Morandi, V.; Marcaccio, M.; Iurlo, M.; Paolucci, F.; Pénicaud, A. Graphene Solutions. *Chem. Commun. (Camb).* **2011**, *47* (19), 5470–5472. https://doi.org/10.1039/c1cc11100k.
(42) Vallés, C.; Drummond, C.; Saadaoui, H.; Furtado, C. A.; He, M.; Roubeau, O.; Ortolani, L.; Monthioux, M.; Pénicaud, A. Solutions of Negatively Charged Graphene Sheets and Ribbons. *J. Am. Chem. Soc.* **2008**, *130*, 15802–15804. https://doi.org/10.1021/ja808001a.
(43) Pénicaud, A.; Drummond, C. Deconstructing Graphite: Graphenide Solutions. *Acc. Chem. Res.* **2013**, *46* (1), 129–137. https://doi.org/10.1021/ar300141s.
(44) Hodge, S. A.; Buckley, D. J.; Yau, H. C.; Skipper, N. T.; Howard, C. A.; Shaffer, M. S. P. Chemical Routes to Discharging Graphenides. *Nanoscale* **2017**, *9* (9), 3150–3158. https://doi.org/10.1039/C6NR10004J.
(45) Milner, E. M.; Skipper, N. T.; Howard, C. A.; Shaffer, M. S. P.; Buckley, D. J.; Rahnejat, K. A.; Cullen, P. L.; Heenan, R. K.; Lindner, P.; Schweins, R. Structure and Morphology of Charged Graphene Platelets in Solution by Small-Angle Neutron Scattering. *J. Am. Chem. Soc.* **2012**, *134* (20), 8302–8305. https://doi.org/10.1021/ja211869u.
(46) Jiang, C.; Peng, Z.; Reyes, C. D. L.; Young, C. C.; Tsentalovich, D. E.; Jamali, V.; Ajayan, P. M.; Tour, J. M.; Pasquali, M.; Martı, A. A. Graphenide Dispersions Aided by Crown-Ethers †. **2017**, 1498–1501. https://doi.org/10.1039/c6cc09623a.
(47) Catheline, A.; Paolucci, F.; Valenti, G.; Poulin, P.; Pénicaud, A. Transparent Electrodes Made from Carbon Nanotube Polyelectrolytes and Application to Acidic Environments. *J. Mater. Res.* **2015**, *30* (13), 2009–2017. https://doi.org/10.1557/jmr.2015.166.
(48) Song, S. H.; Jang, M.-H.; Chung, J.; Jin, S. H.; Kim, B. H.; Hur, S.-H.; Yoo, S.; Cho, Y.-H.; Jeon, S. Highly Efficient Light-Emitting Diode of Graphene Quantum Dots Fabricated from Graphite Intercalation Compounds. *Adv. Opt. Mater.* **2014**, *2* (11), 1016–1023. https://doi.org/10.1002/adom.201400184.
(49) Huang, K.; Delport, G.; Orcin-Chaix, L.; Drummond, C.; Lauret, J.-S.; Penicaud, A. Single Layer Nano Graphene Platelets Derived from Graphite Nanofibres. *Nanoscale* **2016**, *8* (16), 8810–8818. https://doi.org/10.1039/C6NR01512C.
(50) Vecera, P.; Edelthalhammer, K.; Hauke, F.; Hirsch, A. Reductive Arylation of Graphene: Insights into a Reversible Carbon Allotrope Functionalization Reaction. *Phys. Status Solidi Basic Res.* **2014**, *251* (12), 2536–2540. https://doi.org/10.1002/pssb.201451315.
(51) Hof, F.; Schäfer, R. A.; Weiss, C.; Hauke, F.; Hirsch, A. Novel λ 3 -Iodane-Based Functionalization of Synthetic Carbon Allotropes (SCAs)-Common Concepts and Quantification of the Degree of Addition. *Chem. - A Eur. J.* **2014**, *20* (50), 16644–16651. https://doi.org/10.1002/chem.201404662.
(52) Schäfer, R. A.; Englert, J. M.; Wehrfritz, P.; Bauer, W.; Hauke, F.; Seyller, T.; Hirsch, A. On the Way to Graphane-Pronounced Fluorescence of Polyhydrogenated Graphene. *Angew. Chem. Int. Ed. Engl.* **2013**, *52* (2), 754–757. https://doi.org/10.1002/anie.201206799.
(53) Hof, F.; Liu, M.; Valenti, G.; Picheau, E.; Paolucci, F.; Pénicaud,

A. Size Control of Nanographene Supported Iron Oxide Nanoparticles Enhances Their Electrocatalytic Performance for the Oxygen Reduction and Oxygen Evolution Reactions. *J. Phys. Chem. C* **2019**, *123* (34), 20774–20780. https://doi.org/10.1021/acs.jpcc.9b05843.

(54) Liu, M.; Hof, F.; Moro, M.; Valenti, G.; Paolucci, F.; Pénicaud, A. Carbon Supported Noble Metal Nanoparticles as Efficient Catalysts for Electrochemical Water Splitting. *Nanoscale* **2020**, *12* (39), 20165–20170. https://doi.org/10.1039/D0NR05659F.

(55) Tronc, E.; Fiorani, D.; Noguès, M.; Testa, A. M.; Lucari, F.; D'Orazio, F.; Grenèche, J. M.; Wernsdorfer, W.; Galvez, N.; Chanéac, C.; Mailly, D.; Jolivet, J. P. Surface Effects in Noninteracting and Interacting γ-Fe2O3 Nanoparticles. *J. Magn. Magn. Mater.* **2003**, *262* (1), 6–14. https://doi.org/10.1016/S0304-8853(03)00011-8.

(56) Demortière, A.; Panissod, P.; Pichon, B. P.; Pourroy, G.; Guillon, D.; Donnio, B.; Bégin-Colin, S. Size-Dependent Properties of Magnetic Iron Oxide Nanocrystals. *Nanoscale* **2011**, *3* (1), 225–232. https://doi.org/10.1039/c0nr00521e.

(57) Lartigue, L.; Innocenti, C.; Kalaivani, T.; Awwad, A.; Sanchez Duque, M. D. M.; Guari, Y.; Larionova, J.; Gueírin, C.; Montero, J. L. G.; Barragan-Montero, V.; Arosio, P.; Lascialfari, A.; Gatteschi, D.; Sangregorio, C. Water-Dispersible Sugar-Coated Iron Oxide Nanoparticles. An Evaluation of Their Relaxometric and Magnetic Hyperthermia Properties. *J. Am. Chem. Soc.* **2011**, *133* (27), 10459–10472. https://doi.org/10.1021/ja111448t.

(58) Tucek, J.; Sofer, Z.; Bouša, D.; Pumera, M.; Holá, K.; Malá, A.; Poláková, K.; Havrdová, M.; Cepeépe, K.; Tomanec, O.; Zboril, R. Air-Stable Superparamagnetic Metal Nanoparticles Entrapped in Graphene Oxide Matrix. *Nat. Commun.* **2016**, *7*, 12879. https://doi.org/10.1038/ncomms12879.

(59) Peddis, D.; Mansilla, M. V.; Mørup, S.; Cannas, C.; Musinu, A.; Piccaluga, G.; D'Orazio, F.; Lucari, F.; Fiorani, D. Spin-Canting and Magnetic Anisotropy in Ultrasmall CoFe2O 4 Nanoparticles. *J. Phys. Chem. B* **2008**, *112* (29), 8507–8513. https://doi.org/10.1021/jp8016634.

(60) Li, Z.; Wang, S. X.; Sun, Q.; Zhao, H. L.; Lei, H.; Lan, M. B.; Cheng, Z. X.; Wang, X. L.; Dou, S. X.; Max Lu, G. Q. Ultrasmall Manganese Ferrite Nanoparticles as Positive Contrast Agent for Magnetic Resonance Imaging. *Adv. Healthc. Mater.* **2013**, *2* (7), 958–964. https://doi.org/10.1002/adhm.201200340.

(61) Moulder, J. F.; Stickle, W. F.; Sobol, P. E.; Bomben, K. D. *Handbook of X-Ray Photoelectron Spectroscopy: A Reference Book of Standard Spectra for Identification and Interpretation of XPS Data*; Physical Electronics Division, Perkin-Elmer Corporation: Eden Prairie, Minnesota, USA, 1992.

(62) Grosvenor, A. P.; Kobe, B. A.; Biesinger, M. C.; McIntyre, N. S. Investigation of Multiplet Splitting of Fe 2p XPS Spectra and Bonding in Iron Compounds. *Surf. Interface Anal.* **2004**, *36* (12), 1564–1574. https://doi.org/10.1002/sia.1984.

(63) Yamashita, T.; Hayes, P. Analysis of XPS Spectra of Fe 2+ and Fe 3+ Ions in Oxide Materials. *Appl. Surf. Sci.* **2008**, *254* (8), 2441–2449. https://doi.org/10.1016/j.apsusc.2007.09.063.

(64) Biesinger, M. C.; Payne, B. P.; Grosvenor, A. P.; Lau, L. W. M.; Gerson, A. R.; Smart, R. S. C. Resolving Surface Chemical States in XPS Analysis of First Row Transition Metals, Oxides and Hydroxides: Cr, Mn, Fe, Co and Ni. *Appl. Surf. Sci.* **2011**, *257* (7), 2717–2730. https://doi.org/10.1016/j.apsusc.2010.10.051.

(65) Lesiak, B.; Rangam, N.; Jiricek, P.; Gordeev, I.; Tóth, J.; Kövér, L.; Mohai, M.; Borowicz, P. Surface Study of Fe3O4 Nanoparticles Functionalized With Biocompatible Adsorbed Molecules. *Front. Chem.* **2019**, *7* (October), 642/1-16. https://doi.org/10.3389/fchem.2019.00642.

(66) Mørup, S.; Bødker, F.; Hendriksen, P. V.; Linderoth, S. Spin-Glass-like Ordering of the Magnetic Moments of Interacting Nanosized Maghemite Particle. *Phys. Rev. B* **1995**, *52* (1), 287–294.

(67) Chantrell, R. W.; El-Hilo, E. H.; O'Grady, K. Spin-Glass Behavior in a Fine Particle System. *IEEE Trans. Magn.* **1991**, *27* (4), 3570–3578. https://doi.org/10.1109/20.102929.

(68) Bruvera, I. J.; Mendoza Zélis, P.; Pilar Calatayud, M.; Goya, G. F.; Sánchez, F. H. Determination of the Blocking Temperature of Magnetic Nanoparticles: The Good, the Bad, and the Ugly. *J. Appl. Phys.* **2015**, *118* (18), 184304. https://doi.org/10.1063/1.4935484.

(69) Garaio, E.; Sandre, O.; Collantes, J.-M.; Garcia, J. A.; Mornet, S.; Plazaola, F. Specific Absorption Rate Dependence on Temperature in Magnetic Field Hyperthermia Measured by Dynamic Hysteresis Losses (Ac Magnetometry). *Nanotechnology* **2015**, *26* (1), 015704. https://doi.org/10.1088/0957-4484/26/1/015704.

(70) Chikazumi, S. *Physics of Ferromagnetism*; 1997; Vol. 1. https://doi.org/10.1007/978-3-642-25583-0.

(71) Dionne, G. F.; Weiss, J. A.; Allen, G. A. Hysteresis Loops Modeled from Coercivity, Anisotropy, and Microstructure Parameters. *J. Appl. Phys.* **1987**, *61* (8), 3862–3864. https://doi.org/10.1063/1.338621.

(72) Della Torre, E.; Bennett, L. H.; Watson, R. E. Extension of the Bloch T3/2 Law to Magnetic Nanostructures: Bose-Einstein Condensation. *Phys. Rev. Lett.* **2005**, *94* (14), 147210/5-7. https://doi.org/10.1103/PhysRevLett.94.147210.

(73) Cojocaru, S.; Naddeo, A.; Citro, R. Modification of the Bloch Law in Ferromagnetic Nanostructures. *Epl* **2014**, *106* (1), 17001/1-6. https://doi.org/10.1209/0295-5075/106/17001.

(74) Ohresser, P.; Otero, E.; Choueikani, F.; Chen, K.; Stanescu, S.; Deschamps, F.; Moreno, T.; Polack, F.; Lagarde, B.; Daguerre, J.-P.; Marteau, F.; Scheurer, F.; Joly, L.; Kappler, J.-P.; Muller, B.; Bunau, O.; Sainctavit, P. DEIMOS: A Beamline Dedicated to Dichroism Measurements in the 350–2500 EV Energy Range. *Rev. Sci. Instrum.* **2014**, *85*, 013106. https://doi.org/10.1063/1.4861191.

(75) Henke, B.; Liesegang, J.; Smith, S. Soft-x-Ray-Induced Secondary-Electron Emission from Semiconductors and Insulators: Models and Measurements. *Phys. Rev. B* **1979**, *19* (6), 3004–3021. https://doi.org/10.1103/PhysRevB.19.3004.

(76) Brice-Profeta, S.; Arrio, M. A.; Tronc, E.; Menguy, N.; Letard, I.; Cartier Dit Moulin, C.; Noguès, M.; Chanéac, C.; Jolivet, J. P.; Sainctavit, P. Magnetic Order in γ-Fe2O3 Nanoparticles: A XMCD Study. *J. Magn. Magn. Mater.* **2005**, *288*, 354–365. https://doi.org/10.1016/j.jmmm.2004.09.120.

(77) Carvallo, C.; Sainctavit, P.; Arrio, M. A.; Menguy, N.; Wang, Y.; Ona-Nguema, G.; Brice-Profeta, S. Biogenic vs. Abiogenic Magnetite Nanoparticles: A XMCD Study. *Am. Mineral.* **2008**, *93* (5–6), 880–885. https://doi.org/10.2138/am.2008.2713.

(78) Guyodo, Y.; Sainctavit, P.; Arrio, M.-A.; Carvallo, C.; Lee Penn, R.; Erbs, J. J.; Forsberg, B. S.; Morin, G.; Maillot, F.; Lagroix, F.; Bonville, P.; Wilhelm, F.; Rogalev, A. X-Ray Magnetic Circular Dichroïsm Provides Strong Evidence for Tetrahedral Iron in Ferrihydrite. *Geochemistry, Geophys. Geosystems* **2012**, *13* (6), n/a-n/a. https://doi.org/10.1029/2012GC004182.

(79) Jiménez-Villacorta, F.; Prieto, C.; Huttel, Y.; Telling, N. D.; van der Laan, G. X-Ray Magnetic Circular Dichroism Study of the Blocking Process in Nanostructured Iron-Iron Oxide Core-Shell Systems. *Phys. Rev. B* **2011**, *84* (17), 172404. https://doi.org/10.1103/PhysRevB.84.172404.

(80) Thole, B.; Carra, P.; Sette, F.; van der Laan, G. X-Ray Circular Dichroism as a Probe of Orbital Magnetization. *Phys. Rev. Lett.* **1992**, *68* (12), 1943–1946. https://doi.org/10.1103/PhysRevLett.68.1943.

(81) Kallmayer, M.; Hild, K.; Elmers, H. J.; Arora, S. K.; Wu, H.-C.; Sofin, R. G. S.; Shvets, I. V. Magnetic Moment Investigations of Epitaxial Magnetite Thin Films. *J. Appl. Phys.* **2008**, *103* (7), 07D715. https://doi.org/10.1063/1.2838982.

(82) Carra, P.; Thole, B. T.; Altarelli, M.; Wang, X. X-Ray Circular Dichroism and Local Magnetic Fields. *Phys. Rev. Lett.* **1993**, *70* (5), 694–697. https://doi.org/10.1103/PhysRevLett.70.694.

(83) Ankudinov, A.; Rehr, J. J. Sum Rules for Polarization-Dependent x-Ray Absorption. *Phys. Rev. B* **1995**, *51* (2), 1282–1285. https://doi.org/10.1103/PhysRevB.51.1282.

(84) Chen, C. T.; Idzerda, Y. U.; Lin, H.-J.; Smith, N. V.; Meigs, G.; Chaban, E.; Ho, G. H.; Pellegrin, E.; Sette, F. Experimental Confirmation of the X-Ray Magnetic Circular Dichroism Sum Rules for Iron and Cobalt. *Phys. Rev. Lett.* **1995**, *75* (1), 152–155. https://doi.org/10.1103/PhysRevLett.75.152.

(85) Del Bianco, L.; Fiorani, D.; Testa, A. M.; Bonetti, E.; Savini, L.; Signoretti, S. Magnetothermal Behavior of a Nanoscale Fe/Fe Oxide Granular System. *Phys. Rev. B - Condens. Matter Mater. Phys.* **2002**, *66* (17), 174418.

https://doi.org/10.1103/PhysRevB.66.174418.

(86) Bedanta, S.; Kleemann, W. Supermagnetism. *J. Phys. D. Appl. Phys.* **2009**, *42* (1). https://doi.org/10.1088/0022-3727/42/1/013001.

(87) Bødker, F.; Mørup, S.; Linderoth, S. Surface Effects in Metallic Iron Nanoparticles. *Phys. Rev. Lett.* **1994**, *72* (2), 282–285.

(88) Cao, L.; Jiang, Z. X.; Du, Y. H.; Yin, X. M.; Xi, S. B.; Wen, W.; Roberts, A. P.; Wee, A. T. S.; Xiong, Y. M.; Liu, Q. S.; Gao, X. Y. Origin of Magnetism in Hydrothermally Aged 2-Line Ferrihydrite Suspensions. *Environ. Sci. Technol.* **2017**, *51* (5), 2643–2651. https://doi.org/10.1021/acs.est.6b04716.

(89) Lee, E.; Kim, D. H.; Hwang, J.; Lee, K.; Yoon, S.; Suh, B. J.; Hyun Kim, K.; Kim, J. Y.; Jang, Z. H.; Kim, B.; Min, B. I.; Kang, J. S. Size-Dependent Structural Evolution of the Biomineralized Iron-Core Nanoparticles in Ferritins. *Appl. Phys. Lett.* **2013**, *102* (13). https://doi.org/10.1063/1.4801310.

(90) Moon, S.; Shim, I.; Kim, C. Crystallographic and Magnetic Properties of KFeO 2. *IEEE INTERMAG* **2006**, 991. https://doi.org/10.4283/jkms.2007.17.1.038.

(91) Howe, A. T.; Dudley, G. J. Studies of Potassium Ferrite, K1+xFe11O17. II. Mössbauer Effect and Spin Flopping. *J. Solid State Chem.* **1976**, *18* (2), 149–153. https://doi.org/10.1016/0022-4596(76)90089-X.

(92) Ghandour, A. M.; Haggstrom, L.; Edstrom, K. 57Fe Mossbauer Studies of Ba2+-Doped Potassium Ferrite. *J. Phys. Condens. Matter* **1995**, *7* (28), 5657–5663. https://doi.org/10.1088/0953-8984/7/28/019.

(93) Kim, B. H.; Lee, N.; Kim, H.; An, K.; Park, Y. Il; Choi, Y.; Shin, K.; Lee, Y.; Kwon, S. G.; Na, H. Bin; Park, J. G.; Ahn, T. Y.; Kim, Y. W.; Moon, W. K.; Choi, S. H.; Hyeon, T. Large-Scale Synthesis of Uniform and Extremely Small-Sized Iron Oxide Nanoparticles for High-Resolution T 1 Magnetic Resonance Imaging Contrast Agents. *J. Am. Chem. Soc.* **2011**, *133* (32), 12624–12631. https://doi.org/10.1021/ja203340u.

(94) Tromsdorf, U. I.; Bruns, O. T.; Salmen, S. C.; Beisiegel, U.; Weller, H. A Highly Effective, Nontoxic T 1 MR Contrast Agent Based on Ultrasmall PEGylated Iron Oxide Nanoparticles. *Nano Lett.* **2009**, *9* (12), 4434–4440. https://doi.org/10.1021/nl902715v.

(95) Borase, T.; Ninjbadgar, T.; Kapetanakis, A.; Roche, S.; O'Connor, R.; Kerskens, C.; Heise, A.; Brougham, D. F. Stable Aqueous Dispersions of Glycopeptide-Grafted Selectably Functionalized Magnetic Nanoparticles. *Angew. Chemie Int. Ed.* **2013**, *52* (11), 3164–3167. https://doi.org/10.1002/anie.201208099.

(96) Li, Z.; Yi, P. W.; Sun, Q.; Lei, H.; Li Zhao, H.; Zhu, Z. H.; Smith, S. C.; Lan, M. B.; Lu, G. Q. Ultrasmall Water-Soluble and Biocompatible Magnetic Iron Oxide Nanoparticles as Positive and Negative Dual Contrast Agents. *Adv. Funct. Mater.* **2012**, *22* (11), 2387–2393. https://doi.org/10.1002/adfm.201103123.

(97) Boni, A.; Marinone, M.; Innocenti, C.; Sangregorio, C.; Corti, M.; Lascialfari, A.; Mariani, M.; Orsini, F.; Poletti, G.; Casula, M. F. Magnetic and Relaxometric Properties of Mn Ferrites. *J. Phys. D. Appl. Phys.* **2008**, *41* (13), 134021. https://doi.org/10.1088/0022-3727/41/13/134021.

(98) Zhang, H.; Li, L.; Liu, X. L.; Jiao, J.; Ng, C. T.; Yi, J. B.; Luo, Y. E.; Bay, B. H.; Zhao, L. Y.; Peng, M. L.; Gu, N.; Fan, H. M. Ultrasmall Ferrite Nanoparticles Synthesized via Dynamic Simultaneous Thermal Decomposition for High-Performance and Multifunctional T1 Magnetic Resonance Imaging Contrast Agent. *ACS Nano* **2017**, *11* (4), 3614–3631. https://doi.org/10.1021/acsnano.6b07684.

(99) Miao, Y.; Xie, Q.; Zhang, H.; Cai, J.; Liu, X.; Jiao, J.; Hu, S.; Ghosal, A.; Yang, Y.; Fan, H. Composition-Tunable Ultrasmall Manganese Ferrite Nanoparticles: Insights into Their in Vivo T1 Contrast Efficacy. *Theranostics* **2019**, *9* (6), 1764–1776. https://doi.org/10.7150/thno.31233.

(100) Laage, D.; Stirnemann, G.; Hynes, J. T. Why Water Reorientation Slows without Iceberg Formation around Hydrophobic Solutes. *J. Phys. Chem. B* **2009**, *113* (8), 2428–2435. https://doi.org/10.1021/jp809521t.

(101) Hannecart, A.; Stanicki, D.; Vander Elst, L.; Muller, R. N.; Brûlet, A.; Sandre, O.; Schatz, C.; Lecommandoux, S.; Laurent, S. Embedding of Superparamagnetic Iron Oxide Nanoparticles into Membranes of Well-Defined Poly(Ethylene Oxide)- Block -Poly(ε-Caprolactone) Nanoscale Magnetovesicles as Ultrasensitive MRI Probes of Membrane Bio-Degradation. *J. Mater. Chem. B* **2019**, *7* (30), 4692–4705. https://doi.org/10.1039/C9TB00909D.

(102) Vangijzegem, T.; Stanicki, D.; Boutry, S.; Paternoster, Q.; Vander Elst, L.; Muller, R. N.; Laurent, S. VSION as High Field MRI T 1 Contrast Agent: Evidence of Their Potential as Positive Contrast Agent for Magnetic Resonance Angiography. *Nanotechnology* **2018**, *29* (26), 265103. https://doi.org/10.1088/1361-6528/aabbd0.

(103) Petrícek, V.; Dušek, M.; Palatinus, L. Crystallographic Computing System JANA2006: General Features. *Zeitschrift fur Krist.* **2014**, *229* (5), 345–352. https://doi.org/10.1515/zkri-2014-1737.

(104) Galimard, A.; Safi, M.; Ould-Moussa, N.; Montero, D.; Conjeaud, H.; Berret, J.-F. Thirty-Femtogram Detection of Iron in Mammalian Cells. *Small* **2012**, *8* (13), 2036–2044. https://doi.org/10.1002/smll.201102356.

(105) Henoumont, C.; Laurent, S.; Vander Elst, L. How to Perform Accurate and Reliable Measurements of Longitudinal and Transverse Relaxation Times of MRI Contrast Media in Aqueous Solutions. *Contrast Media Mol. Imaging* **2009**, *4* (6), 312–321. https://doi.org/10.1002/cmmi.294.

We show that the Nanocomposite material obtained by mild water oxidation of the reaction product between potassium graphenide and an iron(II) salt consists of ultrasmall potassium ferrite nanoparticles, bound to the graphene nanoflakes. Magnetic and relaxometric properties were show to be widely different from classical ultra-small superparamagnetic iron oxide nanoparticles.

Ferdinand Hof,* Lorenzo Poggini, Edwige Otero, Benoît Gobaut, Mathieu Gonidec, Mathieu Duttine, Patrick Rosa,* Olivier Sandre, Alain Pénicaud

Magnetic ordering in ultrasmall potassium ferrite nanoparticles grown on graphene nanoflakes

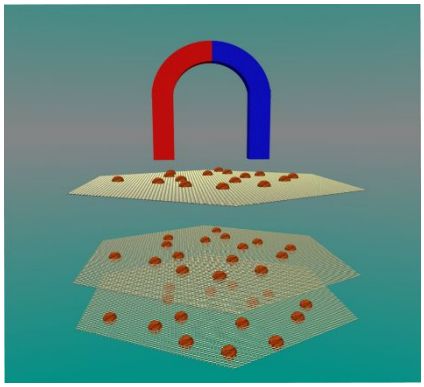

Magnetic ordering in ultrasmall potassium ferrite nanoparticles grown on graphene nanoflakes

Ferdinand Hof, Lorenzo Poggini, Edwige Otero, Benoît Gobaut, Mathieu Gonidec, Mathieu Duttine, Patrick Rosa, Olivier Sandre and Alain Pénicaud

Summary

I. X-ray Photoemission Spectroscopy

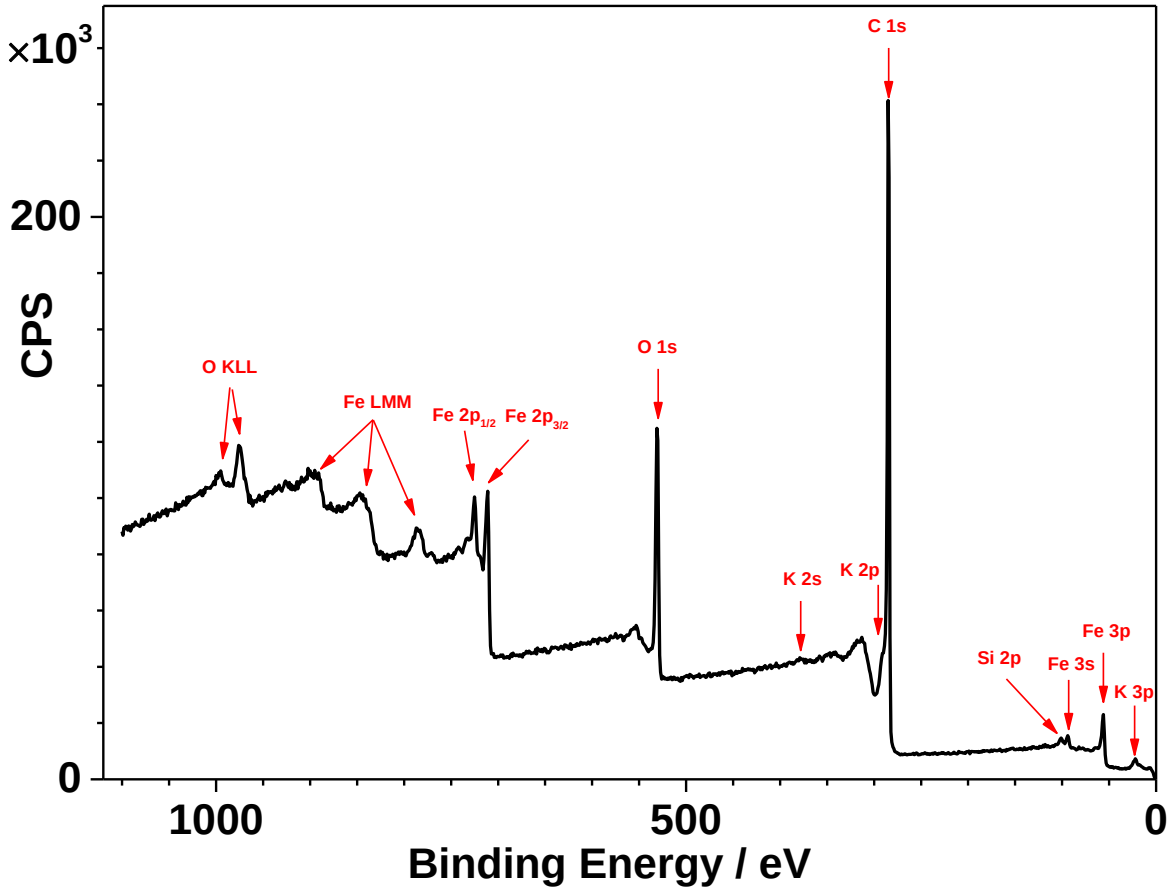

Figure S1. Survey X-ray photoemission spectrum recorded on Fe(nP)/nC.

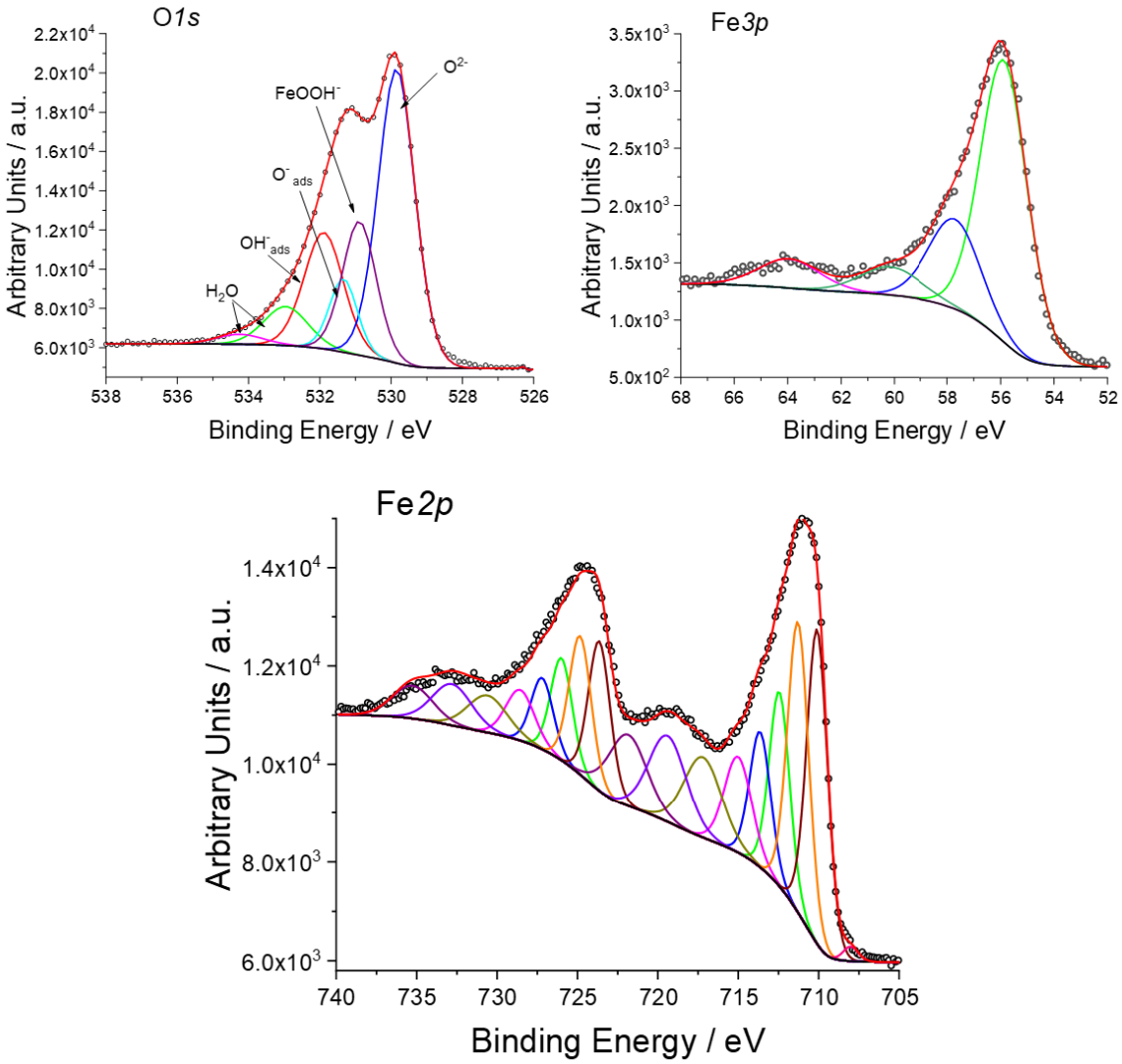

Figure S2. XPS O *1s* (top left), Fe *3p* (top right) and *2p* (bottom) experimental spectra (empty black circles), fitted deconvolution contributions (coloured lines), Shirley backgrounds (black line) and resulting envelope (red line).

BE (eV)	Attribution	Ref
O *1s* spectrum		
529.8	Lattice O^{2-} FeO/FeOOH	[1]
530.9	Lattice OH^- FeOOH	
531.3	Adsorbed O^-	
531.9	Adsorbed OH^-	
533.0	H_2O	
534.3	H_2O	
Fe *3p* spectrum		
55.9	Fe^{3+}	[2]
Fe $2p_{3/2}$ spectrum		
708	pre-peak	[1]
710.1	Fe^{3+} multiplet	
711.4	Fe^{3+} multiplet	
712.6	Fe^{3+} multiplet	
713.7	Fe^{3+} multiplet	
715.1	"surface" peak	
717.3	shake-up	
719.5	shake-up	
721.8	shake-up	
Fe $2p_{1/2}$ spectrum		
723.7	Fe^{3+} multiplet	[1]
724.9	Fe^{3+} multiplet	
726.0	Fe^{3+} multiplet	
727.2	Fe^{3+} multiplet	
728.4	"surface" peak	
730.6	shake-up	
732.8	shake-up	
735.3	shake-up	

Table S1. List of peaks components binding energies (BEs), their interpretation and relevant references.

Please note that the absence of Fe(II) or Fe(0) removes fitting error inherent to mixed species due to spectral overlap.[3]

[1] B. Lesiak, N. Rangam, P. Jiricek, I. Gordeev, J. Tóth, L. Kövér, M. Mohai, P. Borowicz, *Front. Chem.* **2019**, *7*, 642/1.

[2] T. Yamashita, P. Hayes, *Appl. Surf. Sci.* **2008**, *254*, 2441.

[3] M. C. Biesinger, B. P. Payne, A. P. Grosvenor, L. W. M. Lau, A. R. Gerson, R. S. C. Smart, *Appl. Surf. Sci.* **2011**, *257*, 2717.

II. Mössbauer spectroscopy

Table S2. ^{57}Fe Mössbauer hyperfine parameters for each component extracted from the fit of the spectra: isomer shift (δ), quadrupole splitting (Δ) or shift (2ε) and hyperfine magnetic field (B_{hf}). When a distribution of the Δ or B_{hf} parameters was considered, the Lorentzian line width (Γ) was fixed to 0.30 mm/s or 0.40 mm/s. The distribution is then characterized by its mean value (*) and standard deviation (σ). The relative area of each component is also reported.

component	δ	Δ or 2ε	σ	B_{hf}	σ	Γ	**area**
	mm/s	**mm/s**	**mm/s**	**T**	**T**	**mm/s**	**%**
293K							
dDQ	0.35(3)	0.52*	0.22			0.3(-)	31(4)
dS	0.43(5)	0.05(5)	--	39*	11	0.4(-)	69(4)
4.2 K							
dS1	0.47(3)	-0.03(3)	--	51*	3	0.4(-)	81(4)
dS2	0.56(3)	0.06(5)	--	44*	2	0.4(-)	19(4)

III. Magnetometry

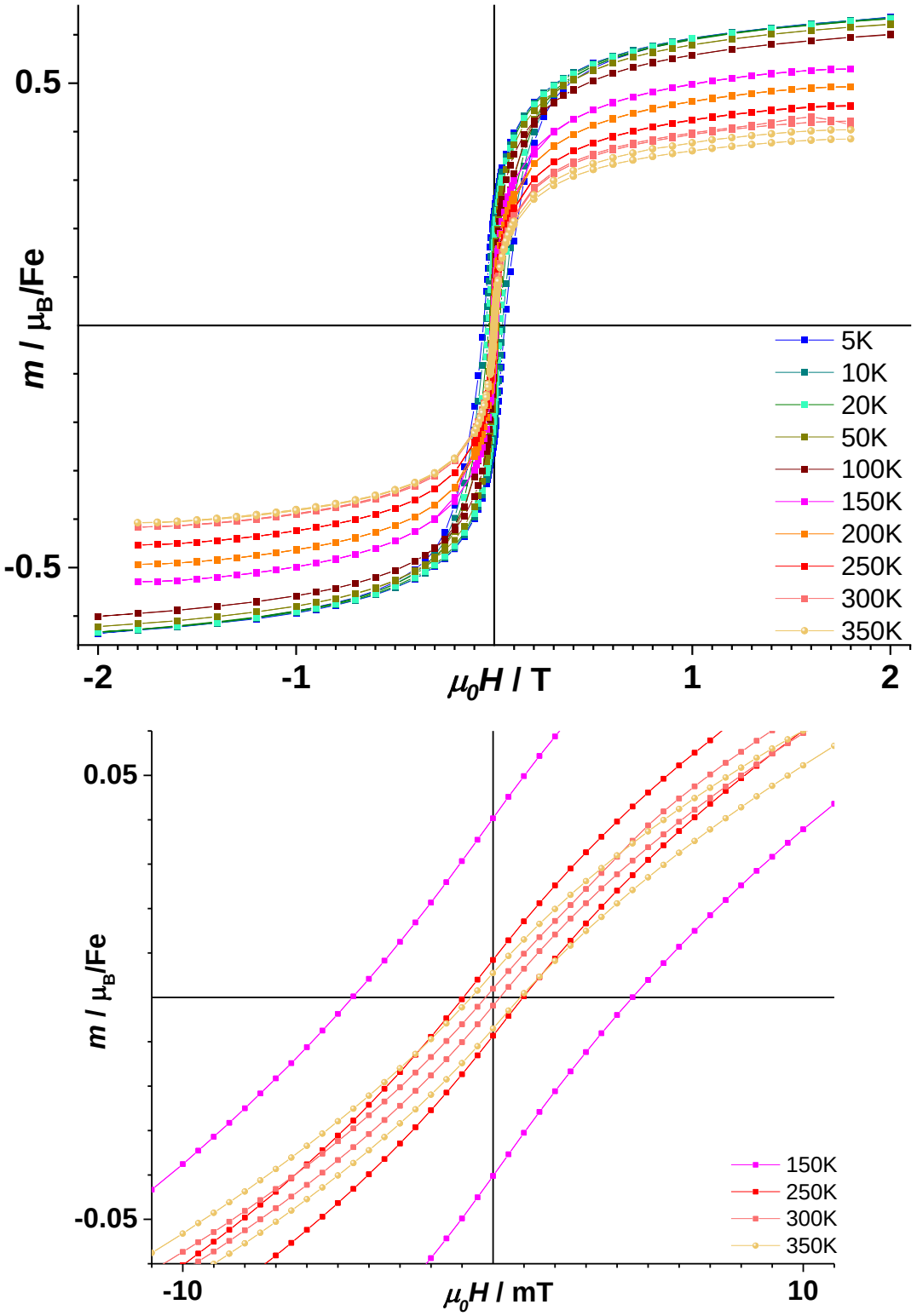

Figure S3. (top) 1st measurement for Fe(mnP)/nC of the field dependence of the magnetization (SQUID measurements up to 2 T, VSM measurements up to 1.8 T); (bottom) close-up around zero field for magnetization curves measured by VSM between 150 and 350 K.

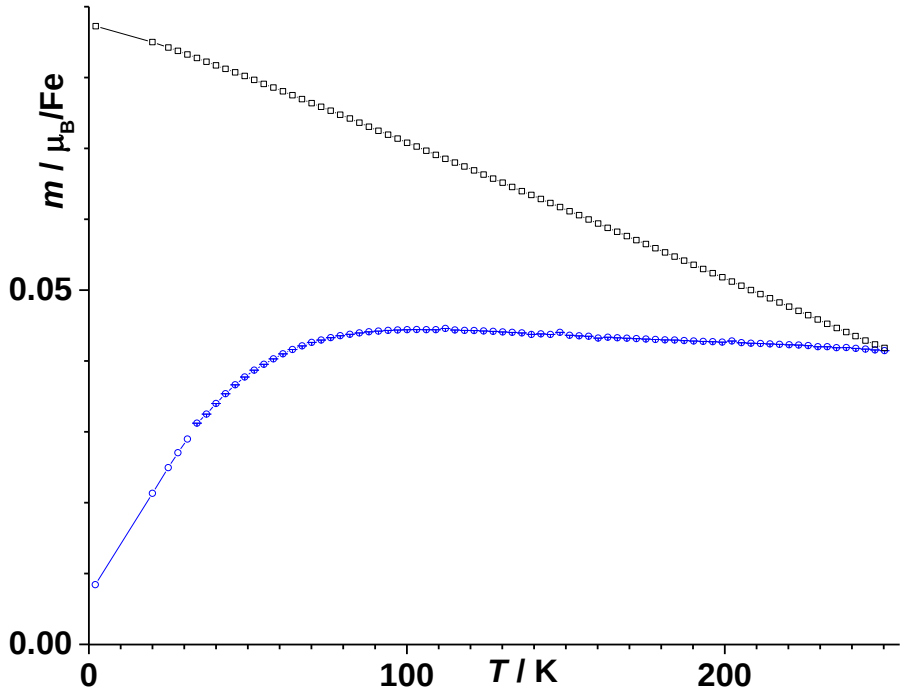

Figure S4. ZFC-FC magnetization (blue circles and black squares respectively) measured at 5 mT for Fe(nP)/nC 2 months after the previous measurement.

Law of approach fit procedure

The following full equation was considered:[4]

$$M(T,H) = M_S(T)\left[1 - \frac{a}{H} - \frac{b}{H^2} - \frac{c}{\sqrt{H}}\right] + \chi_0(T)H$$

In this expression the b/H^2 term is associated with magnetic domains rotation due to the torque exerted by the competition between the external magnetic field and the nanoparticle magnetic anisotropy, and $\chi_0(T)$ is the increase of the spontaneous magnetization that can be linked here as we said with either impurities or the smallest nanoparticles. The a/H term is associated with defects due to dislocations or non-magnetic inclusions and voids,[4] while the $c/\sqrt{H}$ term would result from point-like defects.[5] While b must necessarily be positive, a and c may be linked with an exchange constant and must be of the same sign. Fitting with the whole equation yields results that are heavily correlated and very much dependent on the fitted data range. We thus limited the fit to the 0.4→2 T upwards branch, and cancelled the a and c term: the simplest fits with only the b term were already satisfactory, and the improvement brought by the a and c terms was at the cost of having incoherent signs between the three terms.

Generalized Bloch Law

The saturation magnetization M_S at low temperatures is usually described using the Bloch-Dyson spin wave theory,[6] resulting in the well-known expression

$$M_S(T) = M_S(0)[1 - (T/T_C)^p]$$

where p = 3/2 for bulk ferromagnetic systems. When considering nanostructured materials, deviations are expected due to finite-size effects and a surface-to-volume ratio that cannot be neglected anymore. Corrections were proposed, such as using p close to 2 for nanoparticles[7]. In our case, we were able to fit (R^2 of 0.9876 and 0.9990 respectively, Figure 4) satisfactorily with p = 3/2, that is the value used for bulk ferromagnetic systems.

[4] S. Chikazumi, *Physics of Ferromagnetism*, **1997**.
[5] M. Vazquez, W. Fernengel, H. Kronmüller, *Phys. Status Solidi* **1989**, *115*, 547.
[6] U. Köbler, *J. Phys. Condens. Matter* **2002**, *14*, 8861.
[7] J. L. Dormann, D. Fiorani, E. Tronc, in *Adv. Chem. Phys.*, **1997**, pp. 283–494.

A generalized Bloch law for ferromagnetic nanostructures can be derived analytically considering a Heisenberg spin model taking into account size, shape and surface boundary conditions effects:[8]

$$M_S(T) = M_S(0)\left[1 - BT^{3/2} - FT\ln T - CT\right]$$

with *B* the standard Bloch coefficient for the bulk material, *C* and *F* size, shape and boundary-conditions dependent parameters that can take either positive or negative values.

[8] S. Cojocaru, A. Naddeo, R. Citro, *Epl* **2014**, *106*, 17001/1

Table S3. Saturation magnetization M_S, b and $\chi_0(T)$ term resulting from the law of approach to saturation (LAS) fit, remanent magnetization M_r, coercive field $\mu_0 H_c$ for all measured isothermal magnetization curves, with fit or estimated errors in brackets. No reported error indicates that the value of $\chi_0(T)$ was constrained to follow the linear variation with temperature observed overall.

T (K)	M_S (μ_B/Fe)	b (10^9 $A^{-2}m^2$)	$\chi_0(T)$ (10^{-9} $A^{-1}m$)	M_r (μ_B/Fe)	$\mu_0 H_c$ (mT)
1st measurement (**Figure S3**)					
5	0.5704(6)	18.8(10)	44.5	0.2321(7)	53.9(14)
10	0.567(3)	13.0(9)	45.3(25)	0.207(1)	42.3(6)
20	0.566(4)	13.2(9)	45.0(27)	0.164(10	27.5(3)
50	0.553(3)	13.1(9)	45.9(26)	0.0865(6)	9.21(7)
100	0.5307(9)	14.4(10)	47.2	0.04285(7)	4.51(2)
150	0.470(1)	17.5(14)	48.5	0.04028(7)	3.73(1)
200	0.430(1)	16.9(15)	49.9	0.0225(1)	2.51(2)
250	0.389(4)	12.4(9)	51.9(32)	0.0085(2)	0.96(1)
2nd measurement (**Figure 3** in Main Text)					
1.8	0.552(1)	19.3(9)	55.2	0.22(1)	37(7)
3	0.549(5)	19.3(11)	55.2(37)	0.21(1)	32(2)
5	0.546(1)	19.07(12)	54.9	0.199(5)	26.5(4)
10	0.543(4)	17.1(10)	55.0(29)	0.182(6)	21.5(2)
20	0.541(4)	16.3(11)	54.1(32)	0.12(3)	13(4)
40	0.536(4)	16.1(10)	53.8(29)	0.101(4)	11.4(9)
60	0.527(4)	15.7(10)	53.1(28)	0.0769(8)	8.4(1)
80	0.521(4)	16.1(11)	52.5(31)	0.061(1)	6.3(1)
100	0.513(1)	16.5(6)	52.1	0.050(1)	5.0(1)
125	0.499(4)	16.2(10)	51.9(28)	0.0399(1)	4.23(4)
150	0.485(4)	16.3(11)	51.1(28)	0.0308(1)	3.3(1)
175	0.469(4)	16.1(11)	50.2(27)	0.0213(1)	2.27(7)
200	0.451(3)	16.1(11)	49.1(26)	0.0125(4)	1.32(9)
250	0.413(3)	15.9(11)	47.7(24)	0.0026(8)	0.4(2)

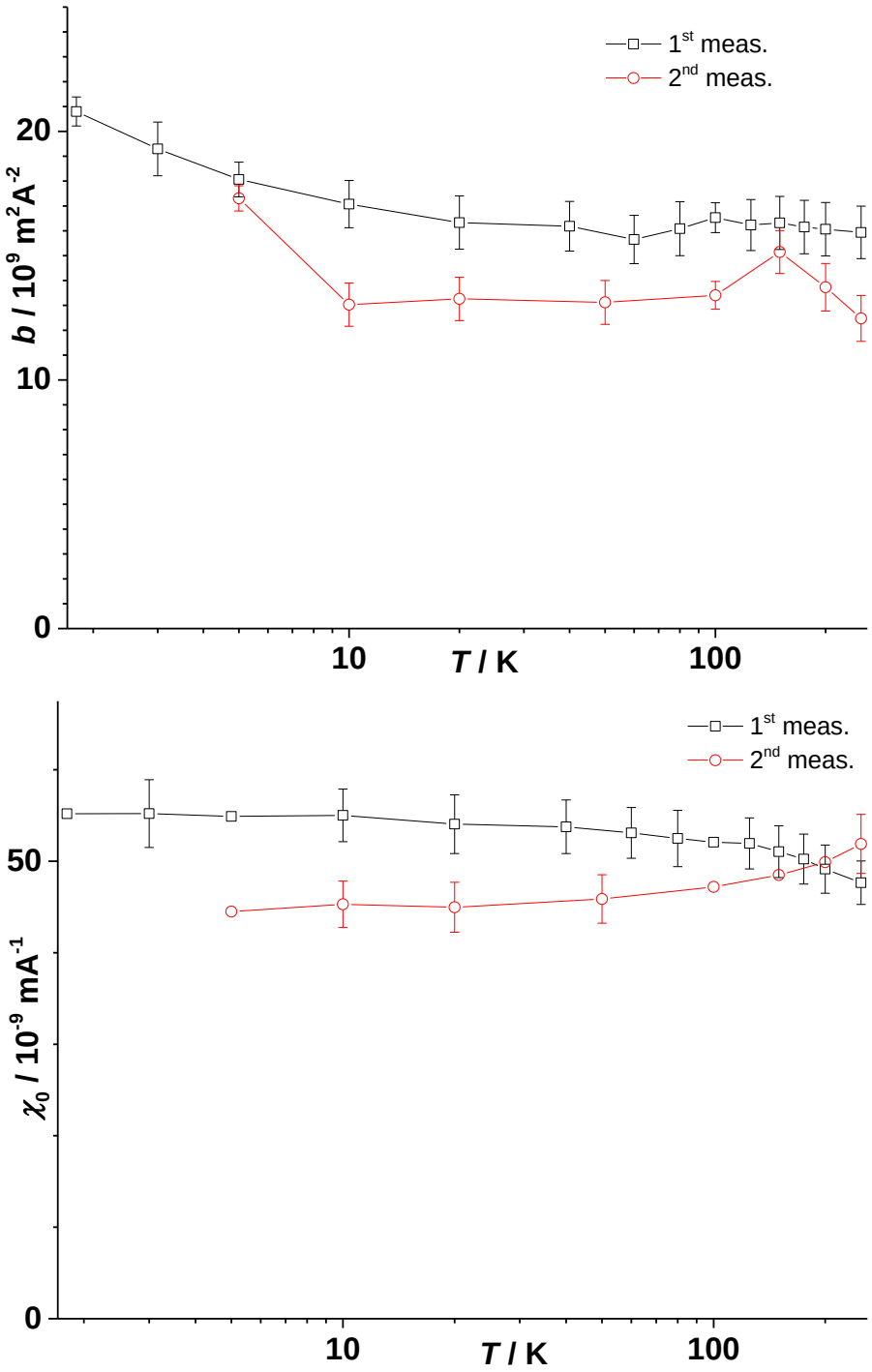

Figure S5. Evolution with temperature of the parameters resulting from the law of approach to saturation fits, b (top) and χ_0 (bottom).

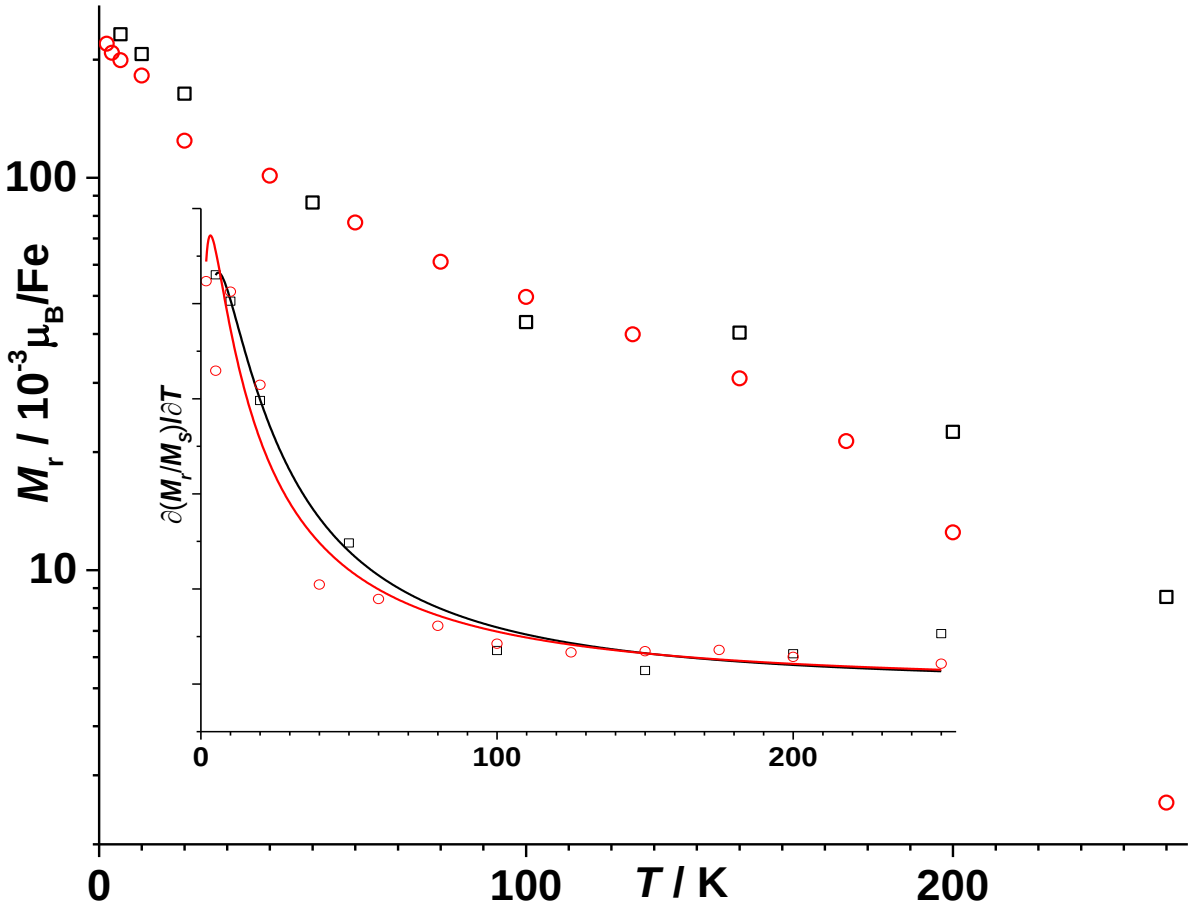

Figure S6. Temperature evolution of remanent magnetization M_r in logarithmic scale. Inset: derivative with temperature of the ratio $M_r(T)/M_S(T)$, and corresponding fits with a log-normal distribution. The 1st measurement is represented as black squares and its fit with a black line, the 2nd measurement as red circles and its fit with a red line.

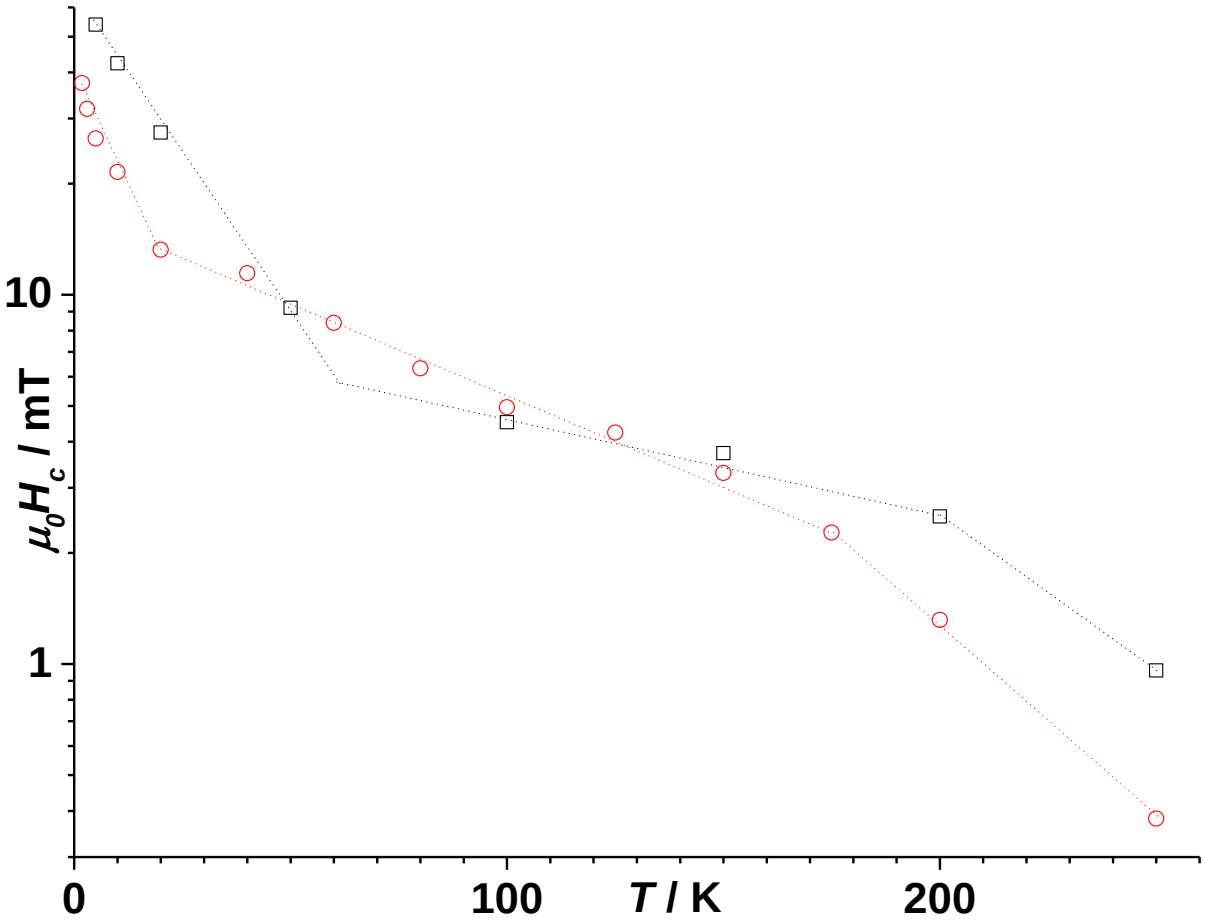

Figure S7. Temperature evolution of the coercive field $\mu_0 H_c$ in logarithmic scale, for the 1st (black squares) and the 2nd measurement (red circles). Dotted lines are guides for the eye.

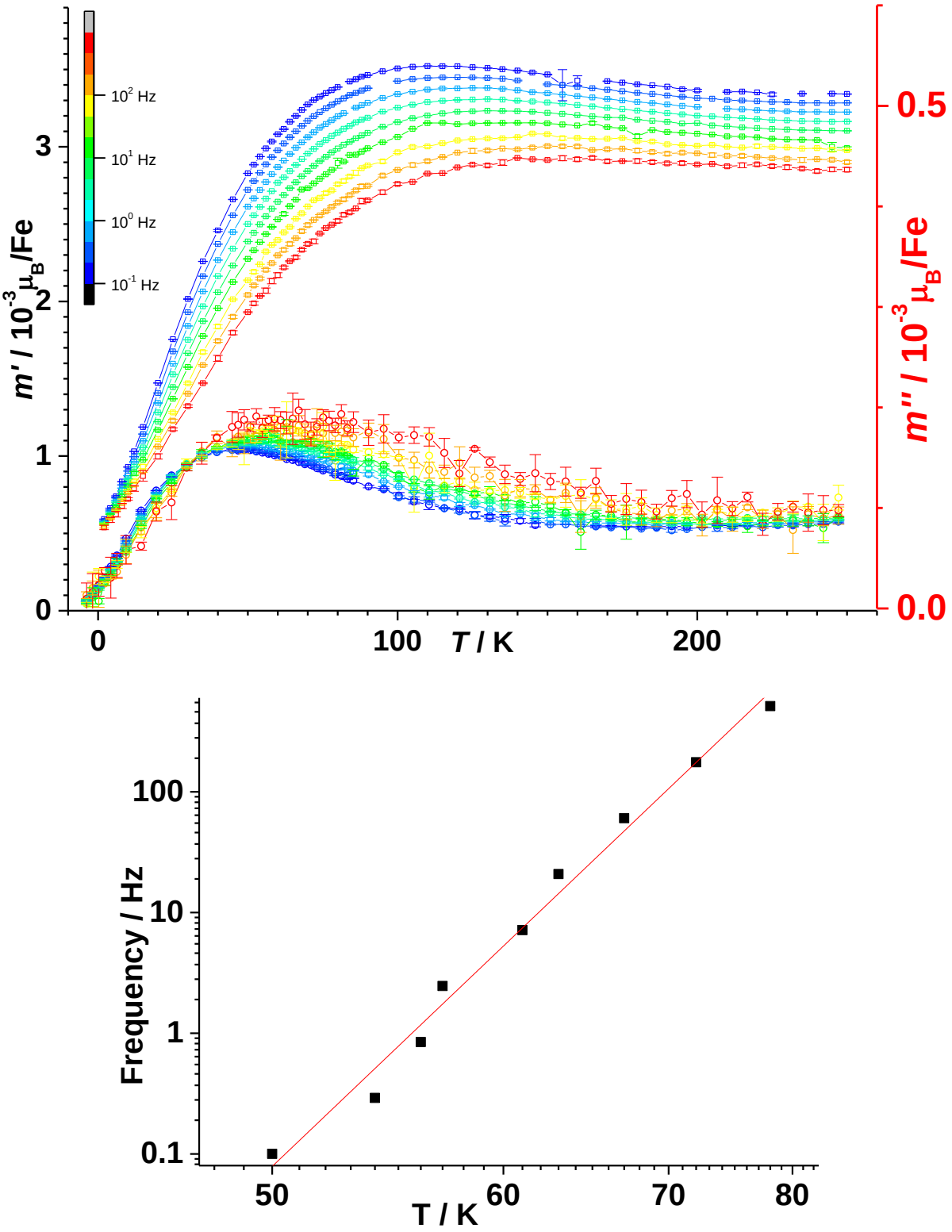

Figure S8. (top) Thermal variation of the first harmonic in-phase (*m'*) and out-of-phase (*m''*) components of the ac magnetic moment under zero-field cooled conditions for Fe(mnP)/nC; (bottom) Arrhenius plot and corresponding linear fit for maxima observed for the out-of-phase component, yielding a slope of 1261(54) K and an intercept of 2.2×10^{-11} s.

IV. X-ray Absorption Spectroscopy and X-ray Magnetic Circular Dichroism

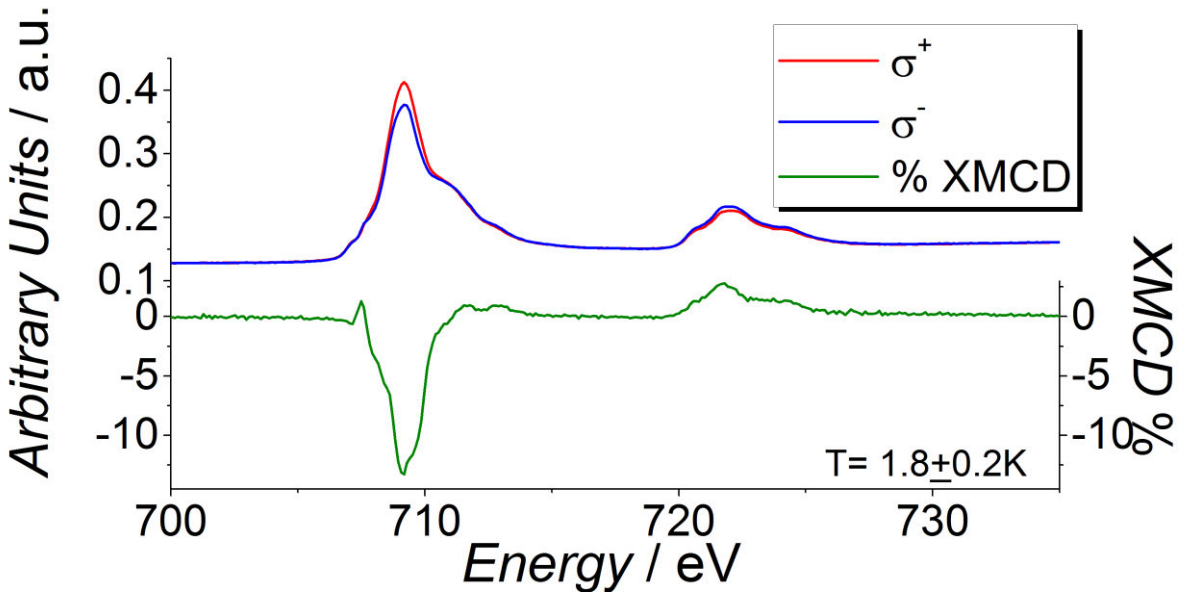

Figure S9. X-ray absorption XMCD measurements of a deposition of FeO nanoparticles measured at 1.8 ± 0.2 K. XMCD (green line) is obtained from the difference right (σ-, blue line) and left (σ+, red line) polarized lights with a saturation field of 2 T.

The FeO Fe(nP)/nC nanocomposites was obtained by a gentle oxidation of the starting Fe(0) Fe(nP)/nC nanocomposites by dosing pure oxygen in the fast entry chamber of the beamline (P_{O2} = 5×10^{-6}mbar, t = 2 min). One can readily see that line shapes for both absorption and dichroic spectra are completely different from the ones measured for Fe(III) nanoparticles.

Table S4. A/B_2 and B_1/B_2 intensity ratio in Fe $L_{2,3}$ XMCD at different temperatures, compared with ratios for ferrihydrite and maghemite.[9]

	A/B_2	B_1/B_2
ferrihydrite[9]	0.52	0.40
maghemite[9]	0.70	0.69
1.8 K	0.62	0.60
4 K	0.59	0.59
60 K	0.60	0.57
150 K	0.65	0.55

[9] Y. Guyodo, P. Sainctavit, M.-A. Arrio, C. Carvallo, R. Lee Penn, J. J. Erbs, B. S. Forsberg, G. Morin, F. Maillot, F. Lagroix, P. Bonville, F. Wilhelm, A. Rogalev, *Geochemistry, Geophys. Geosystems* **2012**, *13*, n/a.

Sum rules

Quantitative information from XMCD data arises from a sum rules analysis, that is based on the integration of the XAS and XMCD spectra.[10] It is then possible to obtain the orbital (m_L) and spin (m_S) magnetic moments on the Fe ion using the following equations:[10]

$$\boldsymbol{m_L = -(6p - 4q)(10 - n_{3d})/r} \quad m_L = -4q(10-n_{3d})/3r \qquad (1)$$

$$\boldsymbol{m_S = -(6p - 4q)(10 - n_{3d})/r} \qquad (2)$$

where m_L and m_S are given in units of Bohr magnetons per cation (μ_B/cation) and n_{3d} is the 3d electron occupation number.[11,12] The n_{3d} values used for the calculation is 5.3 for Fe^{3+} ion as reported in literature.[11,12] The values of p and q were extracted from the integration of the XMCD spectra (see **Figure S10**) and the r value by integrating the isotropic XAS spectra of Fe $L_{2,3}$ adsorption edge (see **Figure S10**) after the subtraction of a step-function background.

[10] C. T. Chen, Y. U. Idzerda, H.-J. Lin, N. V. Smith, G. Meigs, E. Chaban, G. H. Ho, E. Pellegrin, F. Sette, *Phys. Rev. Lett.* **1995**, *75*, 152.

[11] J. A. Moyer, C. A. F. Vaz, D. A. Arena, D. Kumah, E. Negusse, V. E. Henrich, *Phys. Rev. B - Condens. Matter Mater. Phys.* **2011**, *84*, 1.

[12] D. J. Huang, C. F. Chang, H. T. Jeng, G. Y. Guo, H. J. Lin, W. B. Wu, H. C. Ku, A. Fujimori, Y. Takahashi, C. T. Chen, *Phys. Rev. Lett.* **2004**, *93*, 2.

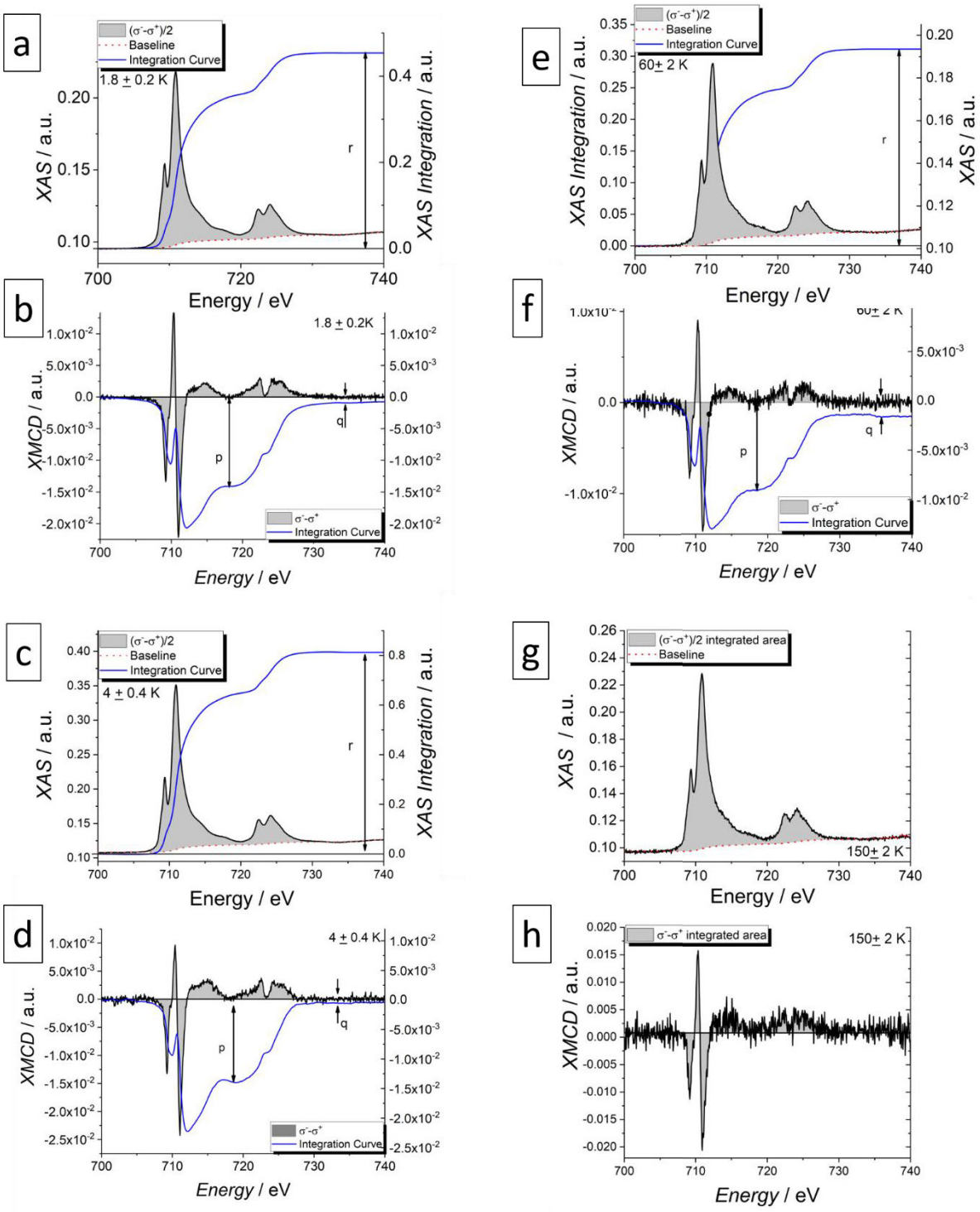

Figure S10. (a,c,e,g,) $(\sigma^{+}+\sigma^{-})/2$ spectra with a double step baseline and the resulting integrated curve corresponding to the gray area; (b,d,f,h) XMCD $(\sigma^{-}-\sigma^{+})$ at four different temperature and the resulting integration (blue line) corresponding to the gray area.

Table S5. Estimation by the sum rules analysis, imposing $n_{3d} = 5.3$, of m_L and m_S at the four different temperatures; the sum rules at 150 K has been performed by fitting the area of the XAS and XMCD spectra.

Temperature	$\boldsymbol{m}_L$ (μB/cation)	$\boldsymbol{m}_s$ (μB/cation)
1.8 K	7E-3	0.52(3)
4 K	5E-3	0.49(2)
60 K	8E-3	0.41(2)
150 K (fit)	1E-2	0.28(1)

V. Demagnetization correction

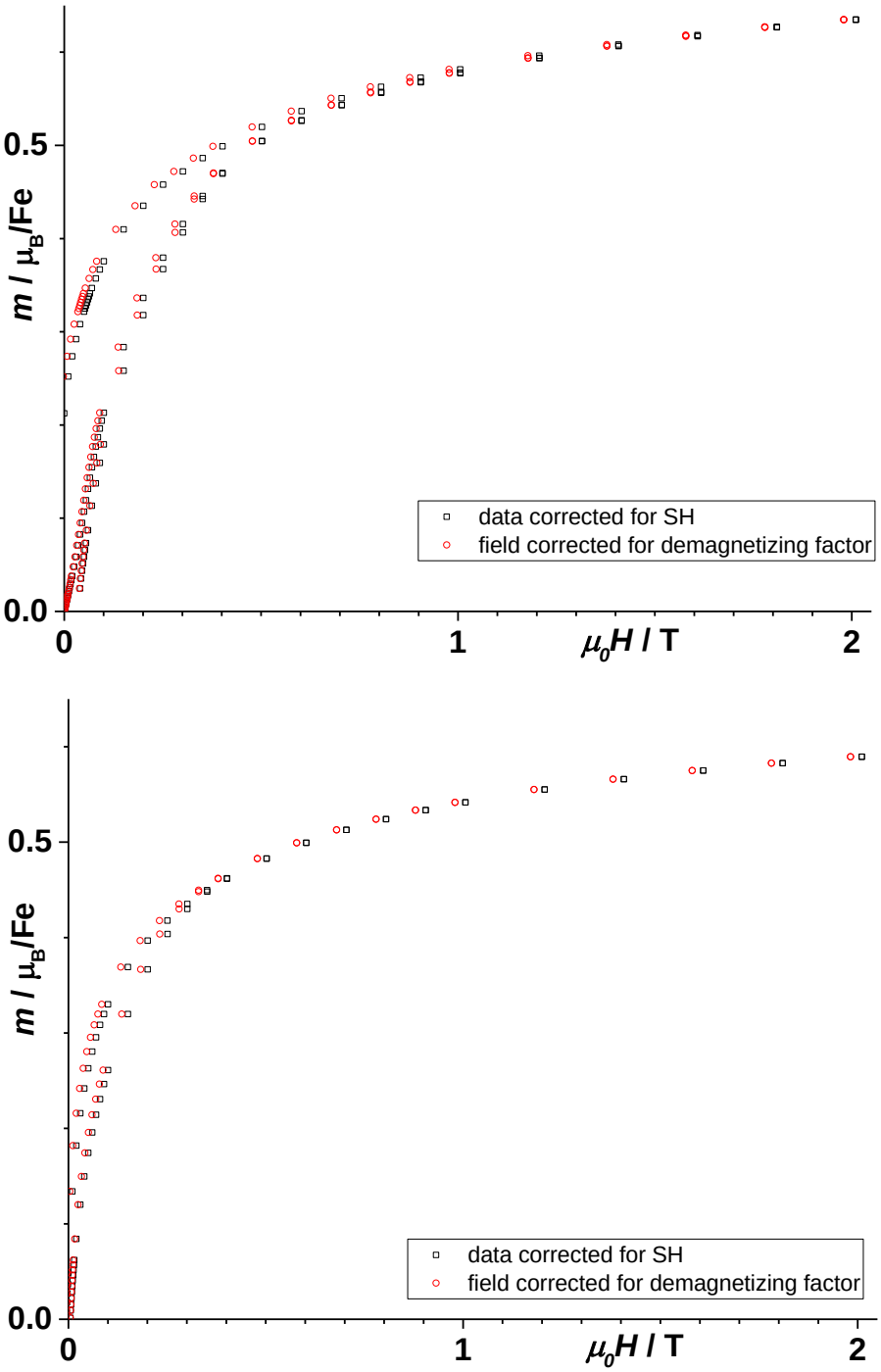

Figure S11. Isothermal magnetization curves at 1.8 K (top) and 100 K (bottom) plotted with the applied field and with the approximated demagnetizing field correction.

VI. [Fe] UV-Vis determination

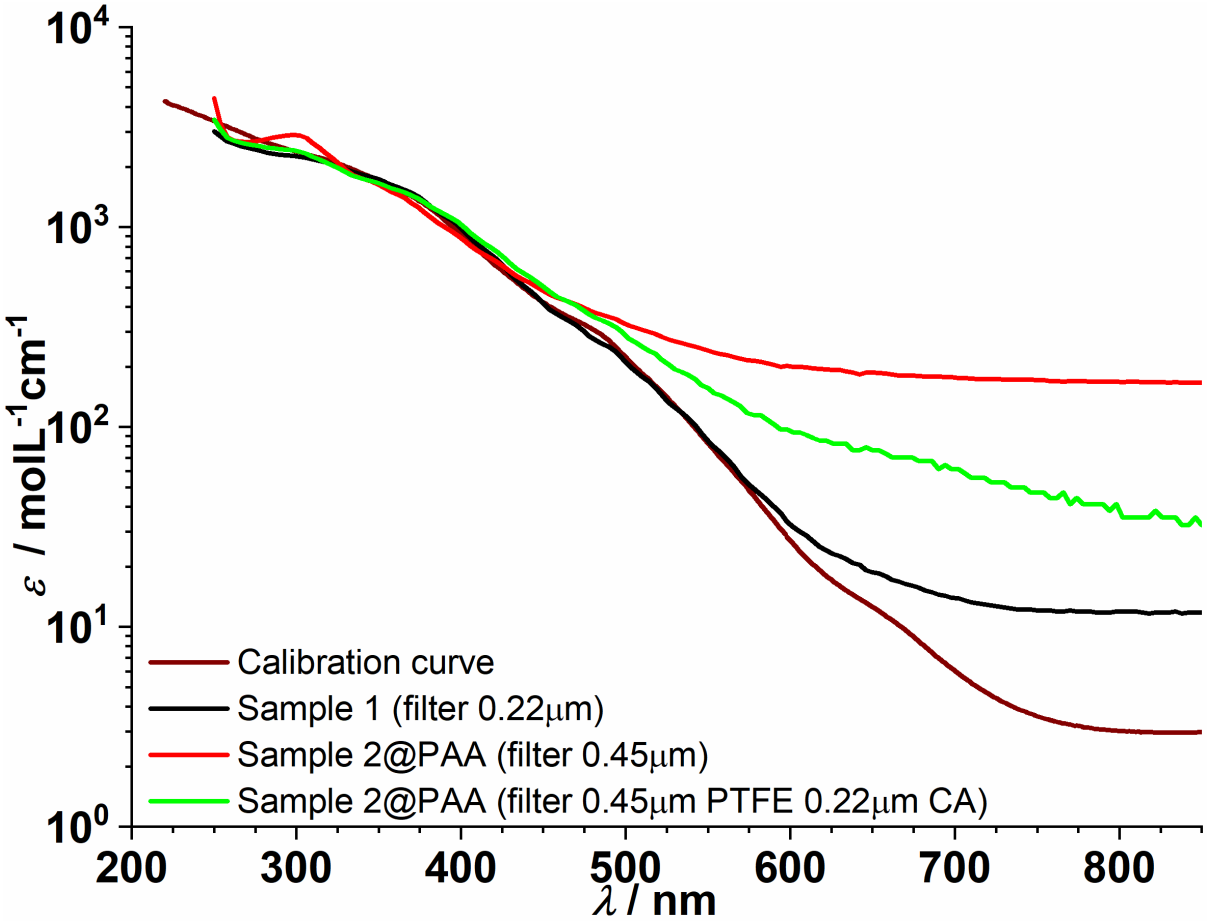

Figure S12. Determination of the equivalent iron concentration by superposing the experimental UV-Vis absorption spectrum between 250 and 850 nm to a reference curve determined by ICP-AES.

VII. Dynamic Light Scattering

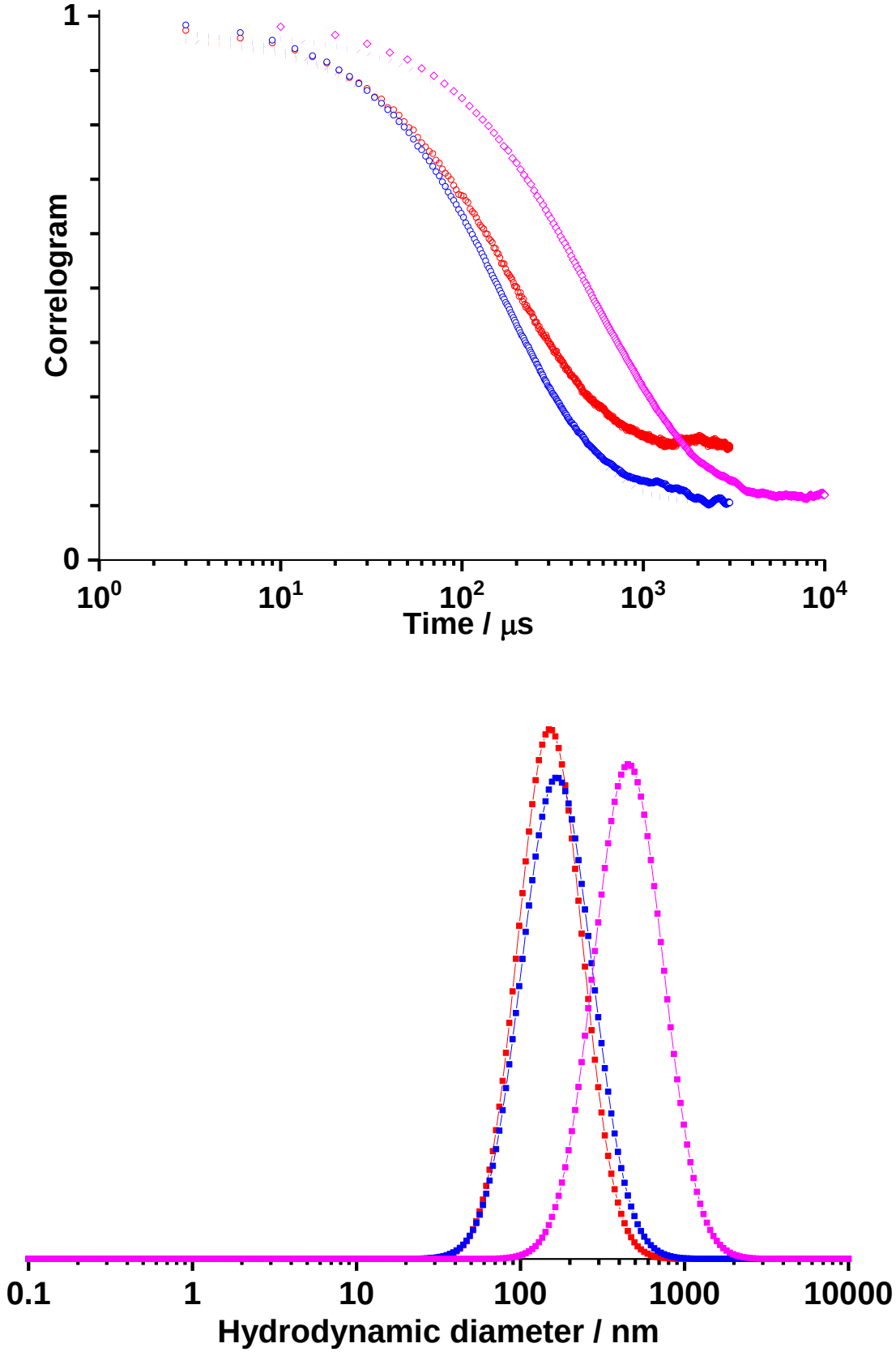

Figure S13. (top) Dynamic Light Scattering autocorrelograms for three samples dispersed in water: sample 1 in PAA (red circles), 0.22μm Cellulose Acetate filter, [Fe]=0.67 mM, d_H=320 nm, PDI=0.26; sample 2 (blue circles), 0.45μm MCM filter, [Fe]=0.40 mM, d_H=114 nm, PDI=0.28; sample 2 in PAA

(violet circles), 0.45μm Cellulose Acetate and 0.22μm PTFE filter, [Fe]=0.17 mM, d_H=112 nm, PDI=0.225. Dotted lines represent the corresponding fits by 2nd order Cumulant analysis. (bottom) Hydrodynamic diameter dispersions resulting from the fits for all three samples.